5-12-2020

The Effect of Chirality on DNA Threading: Exploring Binuclear Ruthenium Intercalators Using Optical Tweezers

Adam A. Jabak
Bridgewater State University

The Effect of Chirality on DNA Threading:

Exploring Binuclear Ruthenium Intercalators Using Optical Tweezers

Adam A. Jabak

Mentor

Dr. Thayaparan Paramanathan

Submitted in Partial Completion of the

Requirements for Departmental Honors in Physics

Bridgewater State University

May 12, 2020

The Effect of Chirality on DNA Threading:

Exploring Binuclear Ruthenium Intercalators Using Optical Tweezers

Adam A. Jabak

Submitted in Partial Completion of the

Requirements for Departmental Honors in Physics

Bridgewater State University

May 12, 2020

[redacted]

Dr. Thayaparan Paramanathan, Thesis Advisor [redacted] Date

[redacted]

Dr. Edward F. Deveney, Committee Member [redacted] Date

[redacted]

Dr. Steven C. Haefner, Committee Member [redacted] Date

Table of Contents

Acknowledgements

Four years ago, I would never had thought that I would be sitting here writing this thesis. My experience at Bridgewater State University (BSU) had not only taught me many remarkable things but had also connected me to many amazing individuals who supported me through tough times, assisted my growth, and believed in me achieving great things. Here I would love to acknowledge many of whom who helped me accomplish towards this project directly and indirectly.

Whenever I reflect to my experiences at BSU, the first image to mind is Dr. Thaya. I foremost deliver my deepest appreciations to you for being my teacher, advisor, and research mentor. You provided me with the strongest support and guidance, helped me achieve higher goals, and inspired me to grow into an ambitious scientist. I thank you Dr. Thaya for motivating me and believing in me, as without you I would not be where I am today.

This project was initially started a few years ago by BSU alumnus Nicholas Bryden who had passed it down to me after his graduation. Thank you for being the working idol in the lab and for also teaching me the basic skills from making flow-cells all the way to setting up the experiment.

I thank all of our collaborators from Williams Lab at Northeastern University, Chalmers Institute of Technology in Sweden, and The Ohio State University for their tremendous help with this project. Thank you, Dr. Mark Williams for giving me the chance to work in your lab for two summers. The opportunity you provided me led to my development as a scientist and opened the gates to many opportunities for me. Thank you, Dr. Micah McCauley for your help in the lab and for providing the DNA used for my experiments. Thank you, Dr. Nabuan Naufer and Dr. Michael

Morse for teaching and guiding me whenever I had got stuck in the lab. I thank Dr. Fredrik Westerlund and Dr. Per Lincoln for synthesizing the molecules we studied and for providing insightful evaluations of our data. Last but not least, I thank our theoretical collaborator Dr. Ioulia Rouzina for taking the time to provide us a better quantitative understanding of our results at my poster during the conference in Peru.

I thank my thesis committee, Dr. Edward Deveney (Dr. D) and Dr. Steven Haefner, for taking the time to read and provide feedback for this document and for also being a critical influence on my experience at BSU. Thank you, Dr. D for supporting me in classes and in the lab; your charismatic approach to teaching physics had dramatically increased my interest in the subject over the past few years. Thank you Dr. Haefner for providing me an opportunity to do research, and for allowing me to work with you as a peer academic leader (PAL) for an introductory chemistry course.

I thank every BSU SMB lab member, past and present, who had contributed anyhow to my learning, development, and success. I especially thank my friends Brian Dolle and Zachary Ells for all the fun times we shared in the lab. You guys brightened each day we spent together at BSU and while travelling across the country and world.

The Physics Department at BSU had also been a critical influence on my entire experience. I thank all of the faculty, students, and staff who made my experience this precious. I thank every professor who taught me fundamental skills in and outside of the classroom. I also a special thank you to Patty Benson for all of her help with administrative needs, purchasing research materials, and of course for all the support and encouragement she provided me.

I thank the whole BSU community, too many individuals to list, for making BSU wholesome and a second home for me. I particularly have been extremely appreciative for the support and attention received from BSU's Boyden Hall. I thank President Frederick Clark for the many times he frankly offered me: "if you ever need anything, come to my office!", Provost Dr. Karim Ismaili for visiting our lab and promoting the FIFA World Cup bracket tournament we held, BSU's Board of Trustees and Chairman Eugene Durgin who had personally honored me at two of their meetings during the entirety of my BSU experience, and BSU's Marketing and Communications Department who have highlighted the lab's success and my achievements multiple times.

I thank BSU's office of Undergraduate Research and the Honors Program for providing me the resources and opportunities needed for research and conference travel. I sincerely thank Dr. Jenny Shanahan for her truly altruistic support for me during my experience at BSU.

I would definitely not have been able to do any research without the generous funding provided to me through both the Adrian Tinsley Program Summer Research Grant and the Bartlett Internship Award. Last year I had the chance to meet president emerita Dr. Adrian Tinsley who's incredible vision two decades ago started BSU's undergraduate research program. I thank her once again for taking that initiative which helped me and many other fellow BSU bears achieve higher academic and career goals. I thank Dean Dr. Kristen Porter-Utley for selecting me for the Bartlett Internship Award, and wholeheartedly thank Mr. and Mrs. Bartlett for their generous support from the Bartlett Internship Award and the Bruce Bartlett '68 Endowed Scholarship which both allowed me the opportunity to do research and focus more on my academics.

I would like to thank my parents and family for the immense support and comfort they provided to me during my secondary education. I am eternally grateful to my mother and father for teaching me to believe in myself and for supporting me to chase my dreams. I thank my brother Rami for his reassuring advice during tough times and for sharing with me his expertise in biochemically labelling DNA in the lab. I also thank my youngest brother Waleed for his inspiring support—always looking up to his brothers as significant role models (I hope that I set a good example). Lastly, I thank my friend Moe Jammal for offering me a strong shoulder to lean on whenever I was in need.

In summary, I thank everyone who helped me over the past few years become who I am today. Without doubt, I would never have achieved any of this without your support.

Abstract

Using optical tweezers, we have been able to study the interactions of small molecules and prospective cancer drugs with DNA. One type of these molecules, known as threading intercalators, has a flat planar intercalating moiety in between the molecule's bulky ancillary supporting ligands. In order to bind with DNA, they have to thread their bulky ancillary ligands in between the DNA base pairs. Due to this requirement for binding, these molecules tend to have high binding affinities and slow kinetics. In this thesis, we explore the binding properties of a ruthenium-based threading intercalator ΛΛ-[μ-bidppz(phen)$_4$Ru2]$^{4+}$, or ΛΛ-P for short. The goal being to compare the binding properties of this complex with the previously studied ΔΔ-P complex, which has the exact chemical components but an opposite chirality (handedness). Our data suggests that left-handed molecules (ΛΛ-P) bind less favorably to DNA with slower binding kinetics and lower binding affinity than the right-handed molecules (ΔΔ-P). These differences are explained by the nano-scale structural changes that occur at the molecular level during the threading intercalation process. This comparison provides us a better understanding of how chirality affects the binding to DNA and will contribute towards improved designs of potential cancer treatment drugs.

Introduction

Is Cancer a Genetic Disease?

Are we close to finding a cure for cancer? That is a tough question to answer; cancer as defined by the American Cancer Society, is a group of diseases which cause cells in the body to change and grow out of control[1]. When a single cell begins undergoing the process of becoming cancerous, it often has altered proteins on its surface that the body's immune system recognizes as "non-self" and destroys it[2]. However, if the cell somehow is able to avoid its destruction, it may proliferate and form a lump known as tumor. Tumors can form anywhere in the body; we know of many different kinds of cancers that commonly affect the lungs, brain, breast, skin, bones or blood.

Generally, the biggest challenge we face is the early detection of cancer. When we identify the symptoms, tumors are spread too far, and it is hard to treat them. Recent studies published in March 2020 as a result of a huge collaboration between Mayo Clinic, Dana Faber Cancer Institute, Cleveland Clinic, The Francis Crick Institute, University College of London and The Woodlands reveals that a DNA-based test from blood samples can help early cancer detection[3]. Figure 1 shows artificially colored cells of pancreatic cancer that can be detected early in its development by analyzing a person's DNA[4]. These results further validate that

Figure 1: Image showing artificially colored cells of pancreatic cancer. (Figure from Ref. 4)

tumors are most commonly a result of genetic mutations, and the classification of cancer as a genetic disease according to the National Cancer Institute[5].

DNA - The Genetic Molecule

When referring to genetics, the term DNA (Deoxyribonucleic Acid) typically comes to mind as the basis of all life. The whole concept of genetics was initially established from a series of experiments in plants performed by Gregor Mendel that described the basic principles of heredity in the mid-1800s[6]. The interest in studying genetics further increased years after Friedrich Miescher was able to isolate a pure sample of DNA in 1869[7]. In the 1920s, Frederick Griffith proposed that DNA was the molecule responsible for inheritance[8]. This idea was further verified in 1944 by experiments done by Oswald Avery that showed DNA was carrying hereditary information[9].

After being known as the hereditary molecule, the next challenge was to discover the structure and function of DNA. Biochemist Phoebes Levene found out that DNA molecules were made up of three components: a phosphate, deoxyribose sugar, and four nitrogenous bases[10]. Levene proposed that these components were linked together forming a complex known as a nucleotide, and the DNA molecule itself was a long string of these nucleotides linked together by their sugars and phosphates. These sugar-phosphate links make up what we know as the DNA backbone. Levene had thought that the four bases came together to form a repeated tetranucleotide throughout the DNA molecule[10]. Later in 1951, Erwin Chargaff showed that this proposal was incorrect when he determined that the amounts of adenine (A) found in a DNA was equal to the amounts of thymine (T), and the amounts of cytosine (C) was equal to the amounts of guanine

(G)[11]. Having equal amounts of each pair suggested that adenine must pair with thymine and cytosine must pair with guanine, which set up Chargaff's rule for base pairing.

The actual structure of DNA was not known until James Watson and Francis Crick used x-ray images taken by Rosalind Franklin and Maurice Wilkins in 1953 to discover the double helix structure of DNA[12,13]. The DNA molecule's structure resembles a twisted ladder (Figure 2)[14] and is commonly referred to as double stranded DNA (dsDNA). The two strands run antiparallel to each other, having complimentary bases in opposite sequence. The complimentary nitrogenous base pairs form the rungs of the ladder, which are separated by 0.34 nm, and the sugar phosphate backbone forms the ladder's rails. As a result of the twisting shape, the DNA molecule has a repeated pattern of major and minor grooves with a distance of about ten base pairs (3.4 nm) per rotation[12]. The ends of strands are labeled as 3' or 5' based on whether they have the terminal sugar link or phosphate group respectively.

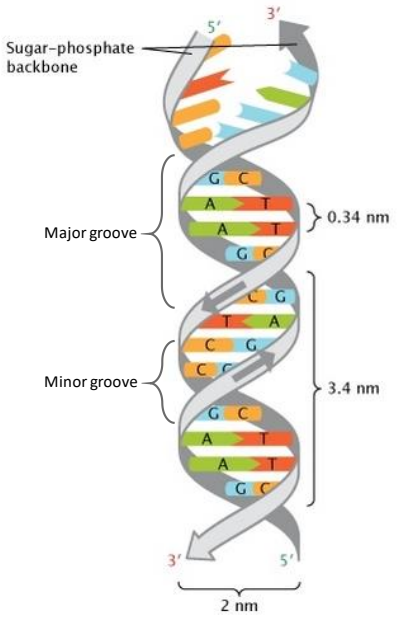

Figure 2: Cartoon representation of the double helix structure of DNA, showing sugar-phosphate backbones (grey) connected by base paring between A-T (green-orange) and G-C (blue-yellow) nucleotides. (Adapted from Ref. 14)

DNA Replication and Transcription

As mentioned in the section above, cellular division in an uncontrollable manner leads to the development of cancer. In order for cells to divide, it is necessary that their genetic information be copied and passed down to the daughter cells. This is known as DNA replication, the process

by which genetic inheritance occurs. During replication the dsDNA molecule is unwound by a motor protein called helicase and is partially separated into two single stranded DNA (ssDNA), opening what is called replication forks[2]. Then another protein called DNA polymerase binds to one of the single strands and reads the base information, adding complementary bases to replicate the DNA. Since the DNA polymerase can only progress in one direction, the replication of the other single strand is done in opposite direction loops in order for a copy to be made. The results in two copies of DNA made out of the parent DNA. Figure 3 shows a simplified illustration of DNA replication to provide a general idea of this complex process[2].

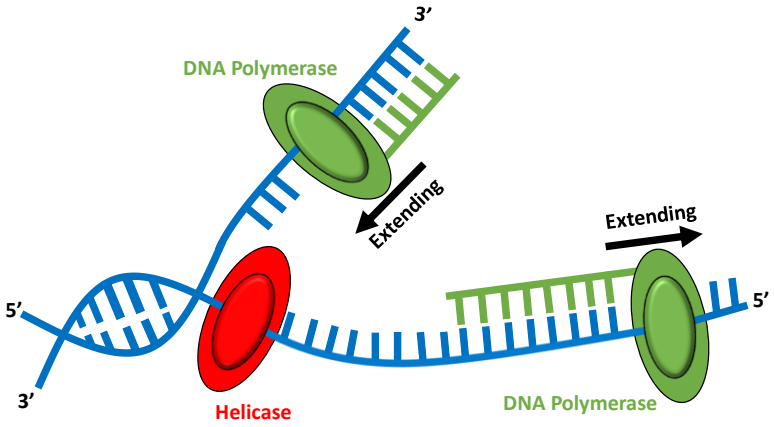

Figure 3: Simplified model of DNA replication fork. Motor protein helicase (red disc) unwinds the dsDNA allowing the DNA polymerase (green discs) to read and replicate the DNA strands.

Transcription, another vital process in the cell, is the process in which RNA (Ribonucleic Acid) are created from sequences of DNA. Figure 4 shows a simplified illustration of how a protein, RNA polymerase, moves along a DNA molecule and create a new RNA molecule. During this process RNA nucleotides that are complimentary to the template DNA strand are

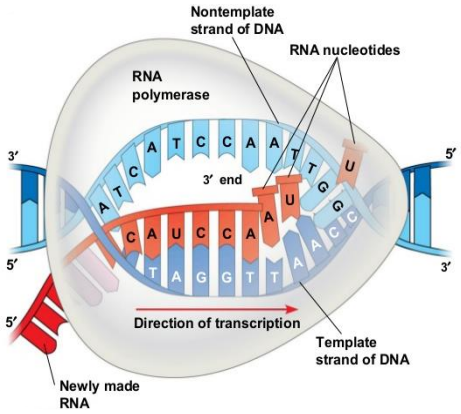

Figure 4: Illustration of RNA polymerase (grey) moving along DNA template strand (dark blue). It joins complementary RNA nucleotides to the 3' end of a growing RNA transcript (orange). (Adapted from Ref. 2)

added one by one to create a new RNA strand[2]. These RNA molecules typically control protein synthesis and regulation, which in fact carry out most cellular jobs.

Targeting DNA with Small Molecules for Cancer Treatment

Small molecules, molecules with molecular weight less than 900 Daltons (approximately 10^{-24} kilograms), are known to interact with DNA to interfere with replication and transcription[15]. These small molecules can inhibit the rapid replication of cancerous cells by binding covalently and noncovalently to DNA. Covalent binding is irreversible, and binding of these molecules perpetually would lead to the inhibition of DNA processes and cell death. Whereas noncovalent binding is a reversible process, meaning given enough time for these molecules to bind to DNA they should also be able to come off. Our emphasis herein will be towards a group of noncovalent binding molecules categorized as intercalators first proposed in 1961 by Leonard S. Lerman[16]. Intercalators are small molecules that have a flat planar section that bind to dsDNA by inserting in between the DNA base pairs (Figure 5)[17].

Figure 5: Intercalator (red) bound between DNA base pairs. (Adapted from Ref. 17)

When these molecules bind to dsDNA, they lengthen the dsDNA as a result of their flat sections stacking with the base pairs; this alters the structure of dsDNA and strengthens it[18]. The dsDNA molecule is strengthened through stacking interactions between the intercalator and the adjacent base pairs above and below it.

In addition, the binding of intercalators to dsDNA can act as a road block to helicase which prevents DNA replication[19] or prevents progression of RNA polymerase during transcription[20]. This

makes intercalation a potential mode to targeting cancer by inhibiting DNA replication or transcription.

Threading Intercalators: A Special Type of Small Molecules

A special type of intercalators, known as threading intercalators, have a dumbbell-shaped design with a flat intercalating moiety in between two bulky ancillary supporting ligands. In order for such molecules to bind to DNA, they must thread one of their bulky ancillary ligand groups through the DNA base pairs so that their middle intercalating moiety can stack between the DNA base pairs. This process requires the opening of at least a base pair in order to allow the threading intercalators to bind[21]. Their slow binding and even slower dissociation rates make them an excellent candidate for anticancer drugs. Nogalamycin which has been used as an anthracycline antibiotic or antitumor drug is an example of a threading intercalator (Figure 6)[22]. Threading intercalators binding to DNA inhibits both DNA replication and transcription[23].

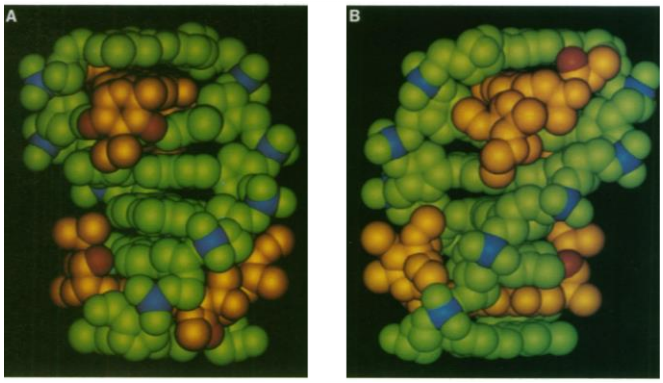

Figure 6: Space filling representations of nogalamycin (gold) bound to DNA (green). The ancillary ligands of Nogalamycin in the picture can be seen popping out in the DNA grooves from different orientations. (Adapted from Ref. 22)

Ruthenium-based Small Molecules as Potential Drugs

Over the past few decades, a large interest has been shown in studying ruthenium-based anticancer drugs. Ruthenium belongs to a special group of the periodic table, called transition metals, and several transition metal-based compounds known to behave as antitumor agents[24]. A

great example of these agents is cisplatin, a commonly used platinum-based cancer drug, that has been around since it reached clinical trials in 1972[25]. Its success had opened the doors for further research in the development of other transition metal-based drugs. Early studies of ruthenium-based DNA binding molecules in 1984 by the Barton Lab[26] shined light towards the development of potential ruthenium-based antitumor drugs that has reached clinical trials[27,28]. Various designs of ruthenium-based complexes which differ by their intercalating moieties were explored by researchers for their binding strength (referred to as binding affinity) to DNA[29]. The results suggested that the binding strength of intercalators depend on the intercalating portion of the complex. Amongst these designs developed, the complexes with dipyridophenazine (known as dppz for short) intercalation moiety exhibited the highest affinity to DNA[30].

Chirality: The Handedness of Small Molecules

In general, all these intercalating complexes have two parts to them; in addition to the intercalating moiety discussed in the above section they have propeller like structures that are known as ancillary ligands. Among the ruthenium complexes with dppz intercalating moiety, the ones with two phenanthroline (phen) ligands, $[Ru(phen)_2dppz]^{2+}$, showed high affinity to

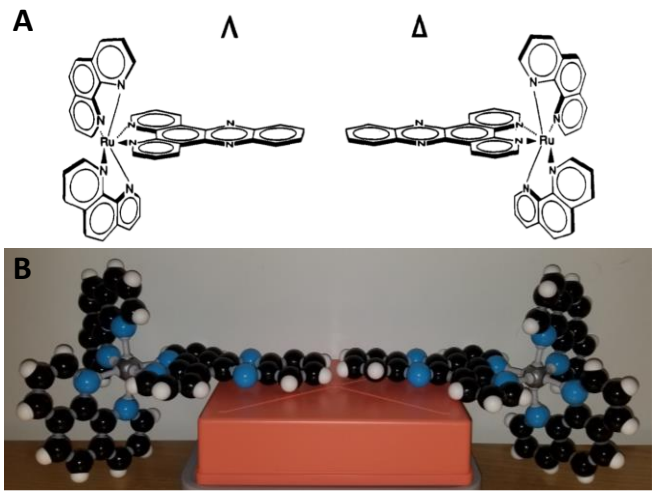

Figure 7: Chemical structure (A) and molecular representation (B) of Λ-P (left) and Δ-P (right) illustrating the mirror image nature of chirality. (Part A adapted from Ref. 31 and Part B is an image of molecular structure built in the lab)

DNA[31]. The two propeller-shaped phen ligands linked off of their central ruthenium atom can differ in orientation as shown in Figure 7.

This orientation, known as chirality, is a property related to the handedness of molecules. Similar to our hands, these molecules are mirror images of each other, and are known as either left-handed (Λ) or right-handed (Δ). Chirality of these molecules can be determined by looking towards the planar section with the ancillary ligands facing away. If the upper side chain is oriented to your right, then the molecule is right-handed (Δ), if the upper side chain is oriented to your left, then the molecule is left-handed (Λ). The chirality is indicated in their formula at the beginning as Δ-$[Ru(phen)_2dppz]^{2+}$ or Λ-$[Ru(phen)_2dppz]^{2+}$, in short referred to as Δ-P and Λ-P respectively going forward (shown in Figure 7).

Threading Binuclear Ruthenium Complexes

The molecules we discussed in previous two sections are centered around a single ruthenium atom and are known as mononuclear complexes. More recently, several of these mononuclear complexes were paired together to design binuclear ruthenium complexes[32-35]. High affinity and slow dissociation kinetics (binding rates) are properties that are considered crucial for antitumor applications.[36]

Based on the high affinities of the mononuclear ruthenium complexes with dppz intercalating moiety, our lab has been focusing on studying binuclear complex designs that adjoin two dppz based molecules. We have previously studied $\Delta\Delta$-$[\mu\text{-bidppz}(phen)_4Ru2]^{4+}$, or $\Delta\Delta$-P for short[21,37], and $\Delta\Delta$-$[\mu\text{-bidppz}(bpy)_4Ru_2]^{4+}$, or $\Delta\Delta$-B for short[38]. These molecules had the same chirality but differed by their ancillary ligands, bipyridine (bpy) in $\Delta\Delta$-B and phen in $\Delta\Delta$-P. The studies using

optical tweezers revealed that the small size difference between the ancillary ligands completely changed the binding mechanism of these two complexes. In addition, the results showed similar binding affinities for both complexes and confirmed the expected faster binding kinetics of ΔΔ-B complex to DNA compared to ΔΔ-P [38].

These binuclear complexes have the intercalating site in the middle with bulky ancillary ligands at the ends, falling under the threading intercalator category we discussed earlier. They exhibit extremely slow binding kinetics and orders of magnitude higher binding affinity compared to the mononuclear complexes, which make them excellent candidates for anticancer drugs[36].

In this study we investigate the binding properties of another binuclear ruthenium-based threading intercalator ΛΛ-[μ-bidppz(phen)$_4$Ru2]$^{4+}$, or ΛΛ-P for short. This molecule has the exact chemical components but an opposite chirality to the previously studied ΔΔ-P complex (Figure 8). Our goal is to determine whether the change in chirality affects the DNA binding properties of these threading intercalators.

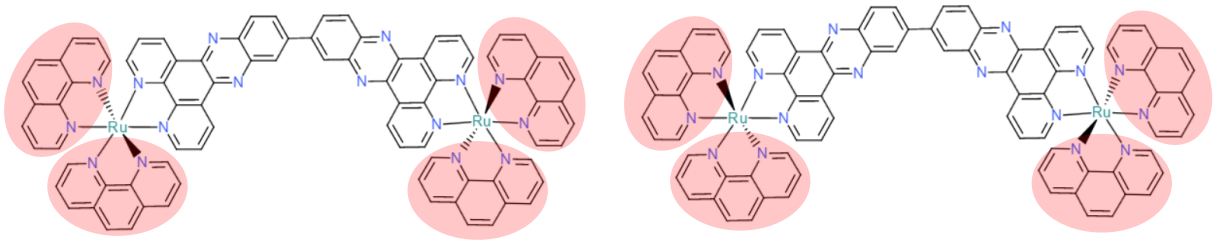

Figure 8: Chemical structures of ΔΔ-[μ-bidppz(phen)$_4$Ru2]$^{4+}$ (left) and ΛΛ-[μ-bidppz(phen)$_4$Ru2]$^{4+}$ (right). The phen ancillary ligands are highlighted in light red. The dark wedges linked from the Ru atoms indicate that the phen is pointed out of the page, whereas the dashed wedges indicate that the phen is pointed into the page.

Probing the Interactions with Single-Molecule Techniques

Previously, these DNA binding binuclear threading molecules have been studied in bulk assays. It has been shown that both ΛΛ-P and ΔΔ-P share a common binding mechanism by binding to DNA grooves in a metastable state before reaching the final threading intercalation state[32,39,40]. The positively charged metal centers of these binuclear threading molecules are initially attracted to the negatively charged phosphate backbone of DNA through stronger electrostatic attractions, which leads to the groove binding.

In contrary to traditional biochemical bulk assays, which perform experiments on population of molecules and provide quantitative information over a collective behavior of the population, there have been techniques developed which can probe these biochemical reactions at the level of individual molecules. These single-molecule techniques have been well adapted to explain molecular interactions and provide precise measurements. In this study we use optical tweezers, one of these popular single-molecule techniques.

Optical Tweezers - Trapping with Light

The idea of optical trapping was first developed by Arthur Askin about five decades ago when he developed a theory to accelerate and trap small particles using the force of radiation pressure[41]. This idea was further developed by Steven Chu et. al. to cool and trap atoms in 1986, and Chu was awarded the 1997 Nobel Prize in Physics for building the first optical trap[42]. The following year in 1987, Arthur Ashkin and his team were able overcome the long-lasting struggle to trap biological samples with lasers without damaging them[43]. They demonstrated this by trapping individual viruses and bacteria with the use of infrared lasers which have wavelengths that water is less likely

to absorb heat. Ashkin had also used optical trapping for manipulating single cells[44] and cell organelles[45], as well as for measuring direct forces from translocating organelles in cells[46]. Unsurprisingly, his contributions towards the development of optical tweezers and its applications to biological systems won Ashkin half of the 2018 Nobel Prize in Physics.

Physics Behind Optical Tweezers

As Ashkin observed, a strongly focused laser beam can catch and hold dielectric particles ranging in sizes from nanometers to micrometers[47]. The idea of optically trapping particles much larger in diameter (micrometer scale for us) than the wavelength of the light used can easily be explained using geometric optics. A particle experiences two forces, a scattering force which pushes it in the direction of the laser propagation and a gradient force that typically pushes it towards the center of the beam.

When a laser beam is used to trap a transparent particle, the rays of the beam that pass through the particle would be refracted at the interfaces of the surrounding and particle. Figure 9[48] illustrates a simple situation when the particle to be trapped is symmetrically located along the optical axis of the microscope An incident ray (blue) travelling through the surrounding medium with index of refraction n_1 reaches the surface of a bead with an index of refraction n_2 at an incident angle θ_1. The ray is then refracted at an angle θ_2 to the normal as a result of Snell's law:

$$n_1 sin\theta_1 = n_2 sin\theta_2 \quad (1)$$

In our case the refractive index of the bead (n_2) is higher than the refractive index of the surrounding (n_1) therefore θ_2 will be less than θ_1 causing the ray to bend towards the normal when it enters the bead (as shown in Figure 9). As the ray leaves the bead, it is also refracted in

according to Snell's Law causing the ray to bend away from the normal. The same applies for the symmetric incoming ray (red) on the opposite side. The change in direction of light rays due to refraction through the bead causes an overall change in the momentum of the photons constituting the beam (top insets in Figure 9). This momentum change gives the direction of force experienced by the photons. If you add these forces created by the two symmetric rays, you can obtain the net force experienced by the photons traversing the rays (bottom left inset in Figure 9). By symmetry, you can say that the total force will be upward pointing away from the focal point of the objective. The force on the bead will be equal and opposite to the force on the photons (bottom right inset). This is known as the scattering force that pushes the bead centered on the optical axis of the objective in the direction of the beam.

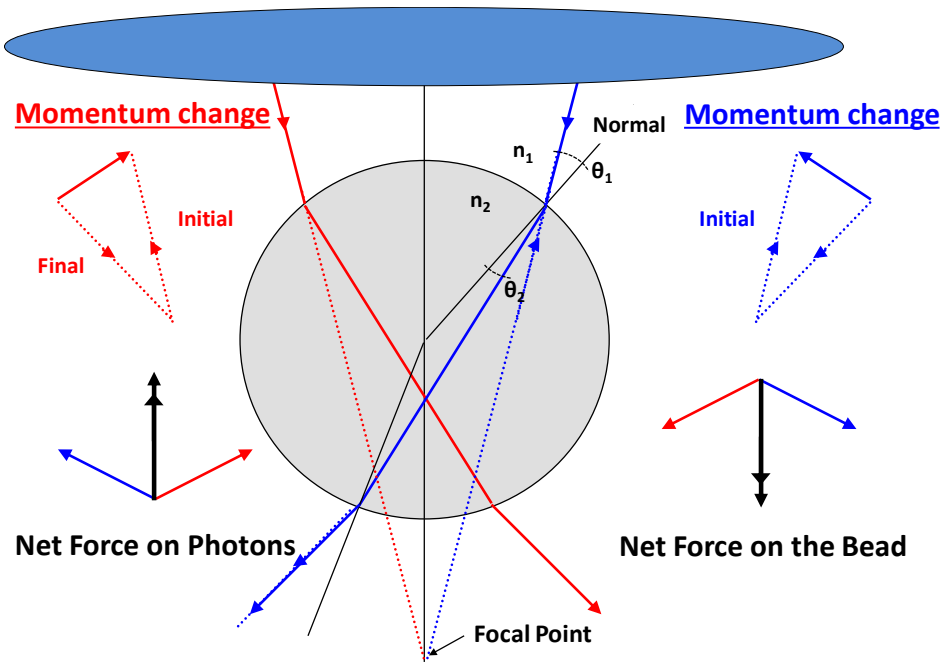

Figure 9: Schematic of scattering forces on a bead centered on the optical axis. Symmetric laser rays (red and blue vectors) emerge from an objective (top oval) and refract through a bead of higher refraction index (grey) causing a change in momentum to the light's photons (top right and left). This change in momentum results in a net force on the photons (bottom left) and in turn creates an equal and opposite force to the bead (bottom right). (Adapted from Ref.48)

On the other hand, if the bead is slightly displaced from the optical axis of the objective, the gradient force comes into action (Figure 10)[48]. The Gaussian profile of the laser creates radially symmetrical distribution of the intensity with maximum intensity being at the center of the beam and dying away towards the edge. The more intense ray from the center of laser beam (darker red ray shown in Figure 10) pushes the bead towards the optical axis and the less intense ray from the edge of the beam (lighter red) pushes the bead away from the optical axis. Since the momentum change caused by the more intense beam is significantly greater than that by the less intense beam the net force of the laser will be towards the optical axis at an angle as shown in Figure 10. The component that pushes the bead towards the optical axis is known as the gradient force and the component that pushes the beam along the optical axis is known as scattering force.

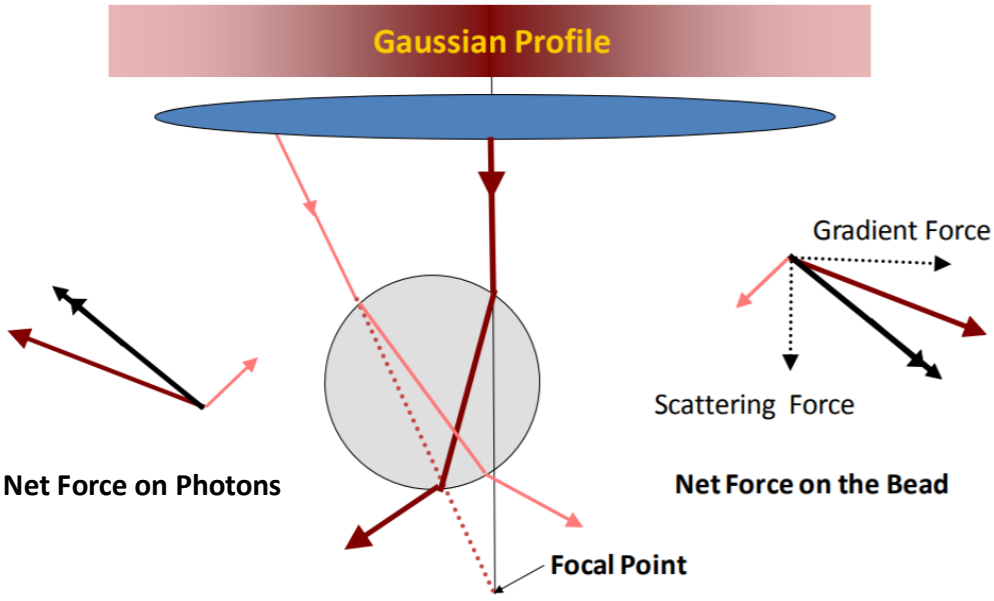

Figure 10: Schematic of gradient force on the bead. The darker ray has greater intensity due to the Gaussian profile of the beam. As the beams are refracted through the bead, the net momentum change in the more intense beam is going to be higher resulting in the net force on photons shown to the left inset. Consequently, the net force on the bead will react equally and oppositely (right inset). This will pull the bead towards the optical axis and push it towards the trap. (Adapted from Ref. 48)

In a dual beam optical tweezers design, there are two counter propagating laser beams that are finely focused to trap the particle. As a result of these two beams, the scattering forces will cancel each other out and the trap is stabilized allowing higher trapping forces[49].

Trapping and Stretching DNA with Optical Tweezers

In 1997, Steven Block's and his research team were the first to trap and manipulate individual DNA molecules using optical tweezers[50]. Even though force measurements and applications on individual DNA molecules had been demonstrated previously using magnetic tweezers[51] and atomic force microscopy[52], optical tweezers allowed for a much larger range of forces, up to 150 pN, that could be applied[53].

The forces exerted in optical tweezers experiments are in the order of piconewtons (pN) which are about a trillion times smaller than the force exerted by the weight of an apple. These forces are in the same order of magnitude as the forces exerted on DNA inside living cells[54]. Typically, in optical tweezers experiments a single dsDNA molecule is chemically attached to a tether and a polystyrene bead or between two polystyrene beads. During the stretching experiments, the tension in the DNA molecule is measured as it is stretched as a function of the extension. Figure 11

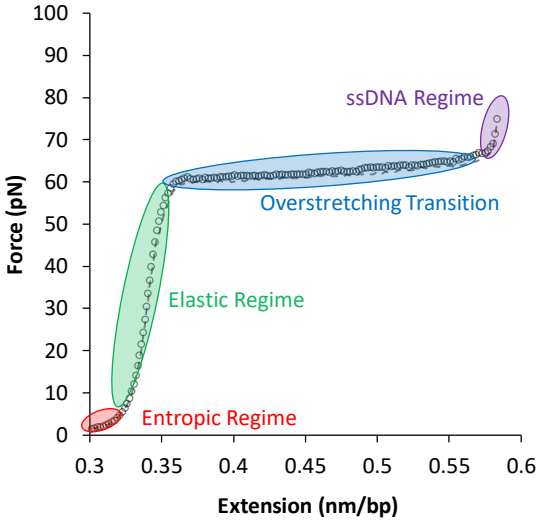

Figure 11: DNA force-extension stretching curve. Highlighted are the four distinct regimes: entropic regime (red), elastic regime (green), overstretching transition (blue), and the ssDNA regime (purple). The open circles and dashed lines represent the stretch curve and the release curve respectively.

shows the force-extension curve obtained from stretching dsDNA that is free to unwind during the stretching (torsional unconstrained).

The dsDNA force-extension curve is divided into four distinct regimes: entropic regime, elastic regime, overstretching transition, and the ssDNA region[55]. The first regime, the entropic regime (highlighted red in Figure 11), shows that minimal force is required to unravel dsDNA as it becomes taut. Beyond this regime, the dsDNA begins to act similar to a rubber band and a larger magnitude of force is required to further extend it. This is known as the elastic regime (highlighted green in Figure 11). After the elastic regime, there is a sudden increase in extension with little force required. This region around 65 pN is known as the overstretching regime (highlighted blue in Figure 11) where we believe there is a disruption of the dsDNA base pairing and stacking interactions resulting in the dsDNA undergoing a force induced melting transition[56-58]. Further stretching leads into the ssDNA regime (highlighted purple in Figure 11) where the dsDNA molecule is now mostly two ssDNA held together by few GC rich regions[18,59].

Visualizing Intercalation in DNA Stretching Experiments

Typical experiments to study the interactions of intercalators have been done by stretching DNA molecules in the presence of the intercalator to obtain a force-extension curve. By observing the changes in the DNA stretching curves, with and without the intercalators, models have been developed to quantify the interactions between the DNA and these molecules[30].

Figure 12 shows experimental data from stretching DNA in the presence of various concentrations of the intercalator ethidium bromide with DNA[15]. The black curve represents the characteristic DNA stretching curve of a dsDNA molecule with no intercalator present. As increasing concentrations of the intercalator are added, several alterations occur. The curves are shifted to the right with the increasing intercalator concentration indicating the lengthening of DNA with more intercalators binding. This lengthening stops when the DNA is saturated with the intercalator. Another interesting feature is the melting force increase, which explains the intercalator strengthening the dsDNA structure and requiring more force to open up the base pairs. The melting transition is also shortened with increasing concentration until vanishing after a critical concentration (125 nM in this case), suggesting that after this concentration the melting of dsDNA is impossible.

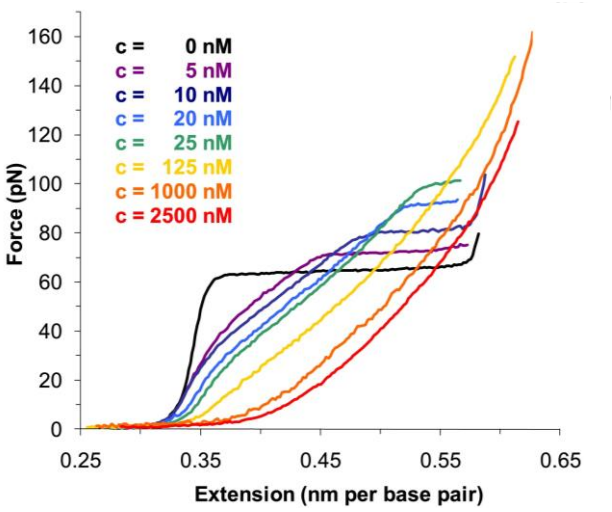

Figure 12: DNA stretching curves in the presence of various concentrations of a classical intercalator ethidium bromide. (Adapted from Ref. 15)

Materials and Methods

Dual Beam Optical Tweezers Setup

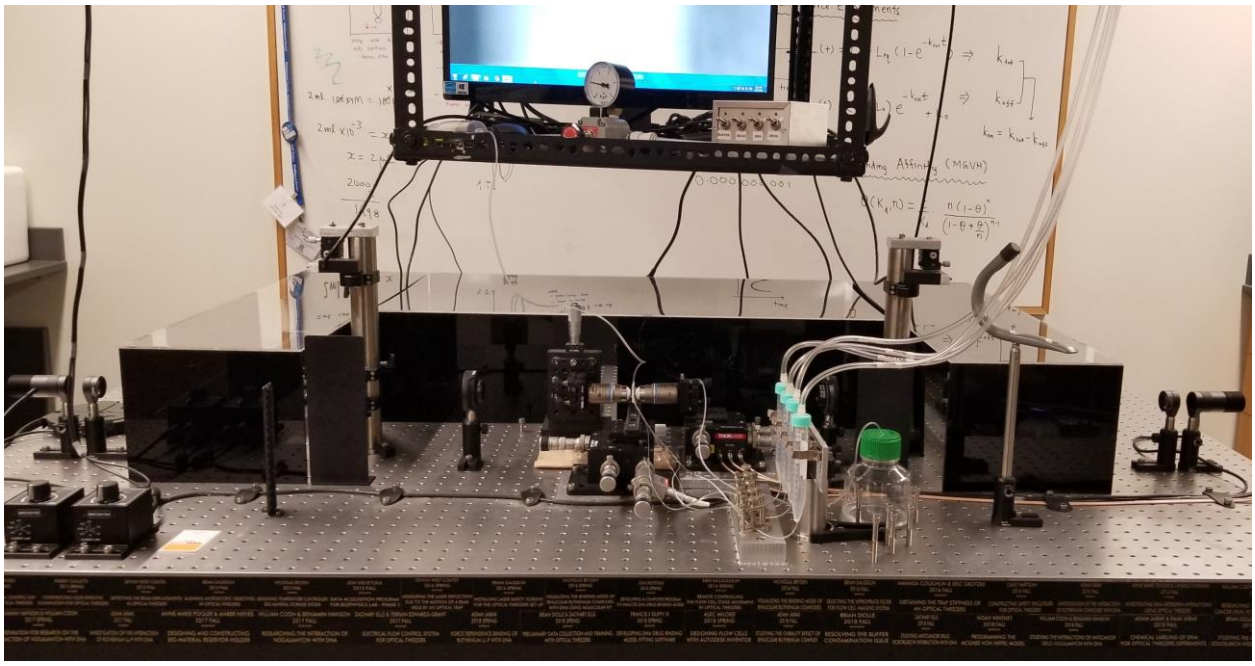

Figure 13: Image of the optical tweezers setup at Bridgewater State University.

We used a dual beam optical tweezers setup (Figure 13) for our experiments, where two counter propagating laser beams are finely focused by microscopic objectives to trap micron-sized objects. The entire set up is built on a heavy optical table that is isolated from ground vibrations using compressed air. This enables us to measure forces in the piconewton range without any interference from vibrations caused by the surrounding. A full schematic showing the beam paths and components of the dual beam setup is shown in Figure 14. In our setup, a single laser beam is split into two separate beams that follow equidistance paths until reaching two microscopic objectives. Each beam must be finely aligned to go through the objective and get focused to a

single spot (within a micron resolution), in a fashion such that when emerging out of the second objective they overlap with the incoming beam travelling in the opposite direction.

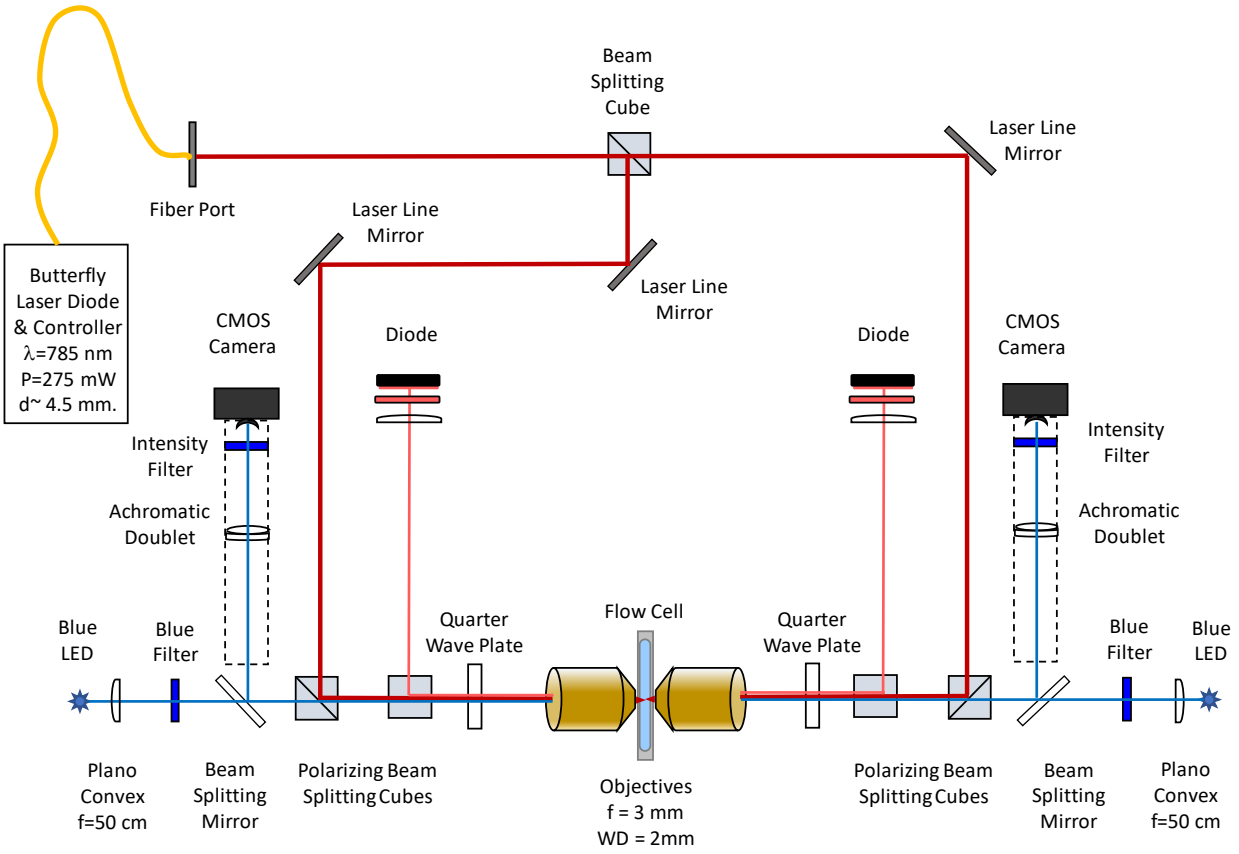

Figure 14: Schematic of the dual beam optical tweezers setup.

We use a butterfly diode laser source (Lumics, LU0786M250) with wavelength 785 nm and power 275 mW, which is linearly polarized and coupled to a fiber port through a Polarization Maintaining fiber (PM fiber). The laser source is maintained at a constant temperature of 25 °C with help of temperature control module (Thorlabs, CLD1015). The fiber port orientation is adjusted to maintain the polarization to be vertical to the optical table.

This beam is then split into two equal power beams by a beam splitting cube. Laser line mirrors are used to reflect and steer the paths of the two beams until reaching polarizing beam splitting cubes. These cubes are made up of two prisms with dielectric beam-splitting coating applied between the hypotenuse planes connecting them. The cubes separate the polarization components by reflecting the set of linear polarization that is parallel to the plane with dielectric coating, while allowing the other polarization to pass. The first set of polarizing beam splitting cubes, on both beam paths are oriented in a way to steer the vertically polarized light towards the objectives. They pass through second set of polarizing beam splitting cubes that do not affect them, as these are oriented to reflect only horizontally polarized light.

The beams continue to go through quarter wave plates which transmit light and modify its polarization. They do so by retarding one component of the polarization by a quarter wave, with respect to its orthogonal component. This allows for the change in polarization of light from linearly polarized light to circularly polarized light and vice versa. Then the now circularly polarized counter propagating beams finally pass through the objectives and into a custom-made glass flow chamber known as the flow-cell (design explained in the next section), where they create the optical trap.

As the beams passes through the flow cell and exit through the second objective, they are steered into a second set of quarter wave plates, which retards one component of the polarization by a quarter wave again, with respect to its orthogonal component. This changes the circularly polarized light into horizontally polarized light (after passing through the two quarter wave plates vertically polarized light is made to be horizontally polarized light). The polarizing beam splitting

cubes that are next to the quarter wave plates are oriented in a way that this horizontally polarized light can be reflected up into position sensing detectors (PSDs). Imperfection of the polarization beam splitting cubes will allow some light to still pass through them. That light travels through the second set of polarizing beam splitting cubes on both sides and onto a beam splitting mirror that guide them towards the cameras. This allows us to image the laser spot and visualize the optical trap on a computer screen.

A blue LED source is used from either side to illuminate the flow-cell and focused inside a CMOS camera allowing us to see around the optical trap inside the flow-cell. Since the blue light from LED is randomly polarized, it can pass through all of the optical components.

Flow-cell Design

All of our experiments took place in an airtight house-built small flow chambers that we call flow-cells (Figure 15). The flow-cell is constructed out of a custom cut Plexiglas spacer with an open channel in the middle and three machine drilled canals (one on each side and one on the top) leading into the middle channel. This spacer is sealed by two glass cover slides (Thermo

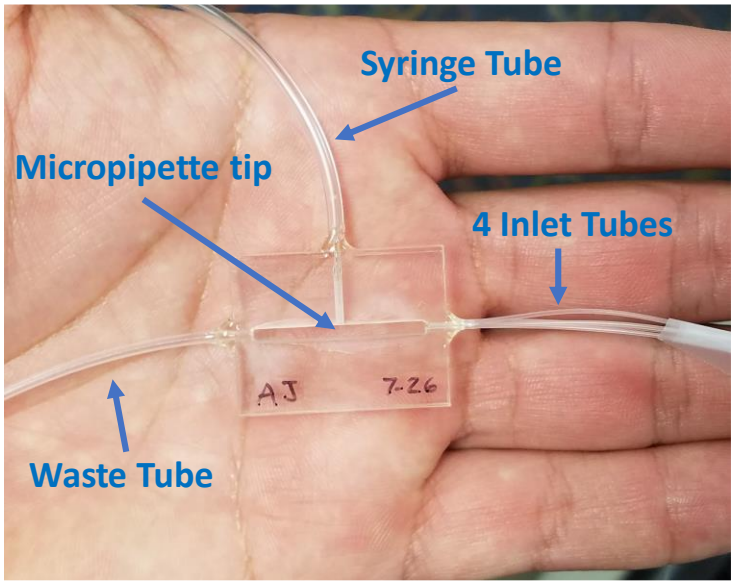

Figure 15: Custom made flow-cell designed for optical tweezers experiments. A micropipette tip is inserted through the vertical canal and connected to a syringe. Four inlet tubes are inserted (right) to allow the flow of buffer, beads, DNA, and the studied drug into the chamber which then are flowed out and collected by a waste tube inserted from the opposing side.

Scientific G CVRGLS NO 1 30X22 mm) from each side using an optical adhesive (Norland Products 6801) and cured with UV light (whenever we use the optical adhesive we allow it to cure for 15-20 minutes under UV light).

A borosilicate glass micropipette tip (World Precision Instruments TIP1TW1) is inserted through the top machined drilled canal down into the flow channel such that the tip is just before the middle of the channel. This insertion requires great precision as any minor bumping of the tip will cause it to shatter, therefore carefully done with the help of a microscope and very steady hands. After inserting the tip, the region where the tip enters the canal is sealed with optical adhesive. A diamond engraver pen is used to fragment off the excessive length of the micropipette tip, leaving between 0.5 – 1 cm of the tip outwards. This small stub is inserted into a tubing (0.050" ID x 0.090" OD, Cole-Parmer EW-06419-05) and sealed again with the adhesive. This tubing is later connected to a syringe during the experiments to apply suction in the tip.

Four inlet tubes (0.011” ID and 0.024” OD, VWR International 63019-004) are inserted through one of the drilled holes on one side of the flow-cell and sealed with the optical adhesive. These inlets allow for the flow of buffer, beads, DNA, and the intended drug to be studied into the flow-cell. A waste tube (0.045” ID and 0.062” OD, VWR International 63019-128) is inserted through the drilled hole on the opposite end and sealed with the optical adhesive. This outlet leads to the collection of the waste in a separate container. The construction of each flow-cell typically takes around four hours to build and each typically last only for several experiments before needing replacement.

Setting up the Flow-cell

We must follow numerous steps and have consistent preparation methods everytime we plan to set up our experiments. We first begin connecting a flow-cell to custom-made reservoir tubes that will hold volumes of the various biomaterials needed for our experiments. Figure 16 shows the reservoir tubes that hold our biomaterials needed for the experiments. The bottom of each reservoir tube is sealed to a tubing (0.020" ID and 0.060" OD, Cole-Palmer EW-06419-01) that goes through a valve to allow or block the flow of the biomaterials. The tubing is then connected to one of the inlet tubes of the flow-cell.

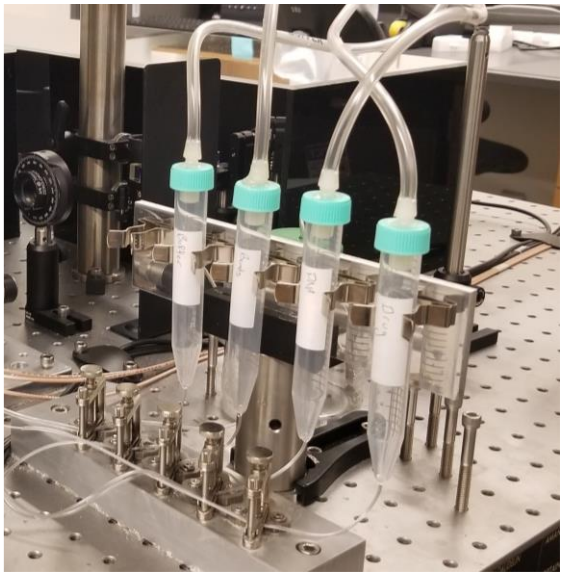

Figure 16: Reservoir tubes that house our biomaterials used in experiments labelled for buffer, beads, DNA, and drug.

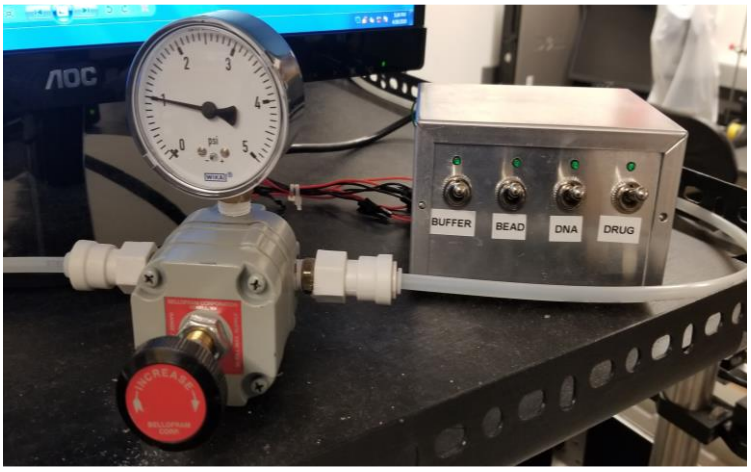

Figure 17: Electrical flow control box to control the flow of buffer, beads, DNA, and drug into the flow-cell. Compressed air is used to apply pressure on the biomaterials inside the reservoir to push them through the tubings into the flow-cell for the experiments.

The lids of the reservoir tubes are connected to a compressed air system so that pressure can be applied to flow the biomaterials into the flow-cell. This air pressured system uses a set of solenoids that are controlled by a custom-made electrical flow control box to switch between different biomaterial flows (Figure 17).

Cleaning up the Flow-cell

After setting up the flow-cell, around 2 ml buffer solution that mimics the physiological conditions found within the body's cells (100 mM Na^+, 10 mM TRIS, pH 8) is flowed through each reservoir in order to clean out any dust or contaminants in the system. All of the air from the tubing and flow-cell is then removed by filling the flow-cell by flowing in buffer from each reservoir tube and gently tapping to get rid of any air bubbles. Then the flow-cell is carefully docked in between the objectives onto a holder housed on a piezoelectric controlled stage (Figure 18).

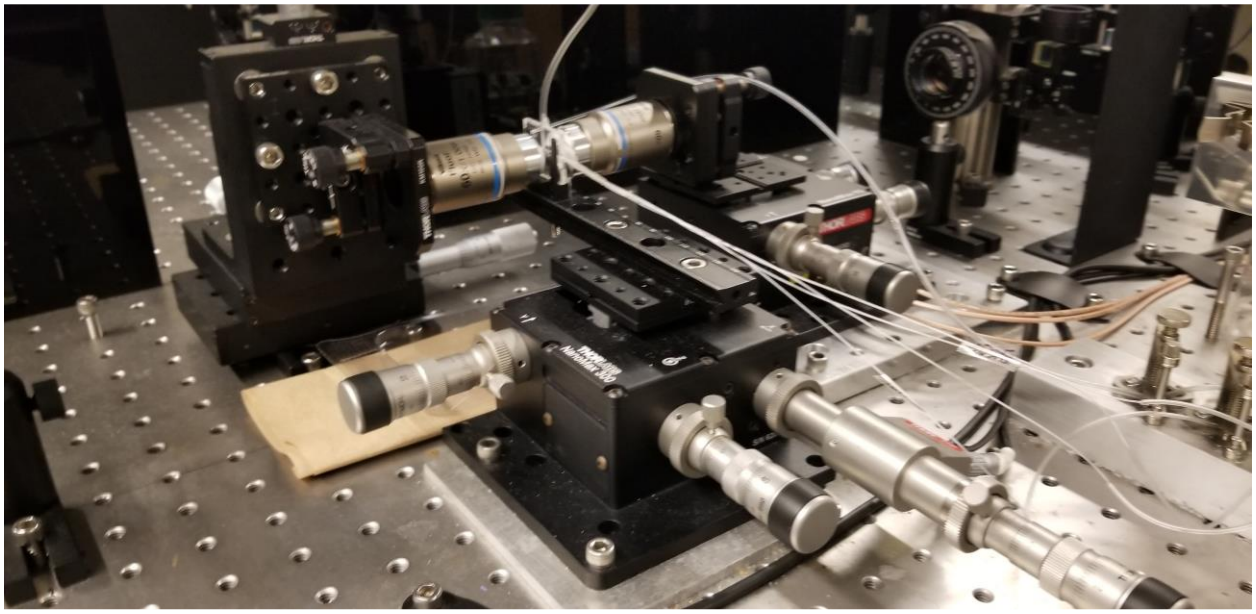

Figure 18: Image showing a flow-cell docked in between objectives onto a holder housed on the piezoelectric controlled stage.

Basic Laser Alignment

The next step of the preparation process is our daily laser alignment. We start by turning on the temperature control module for the laser and wait until it reaches the set temperature of 25 °C and then turn the laser on. Next we turn on one of the cameras and the opposing blue LED source to illuminate the flow cell. This will project a magnified image of the experimental area on a display screen.

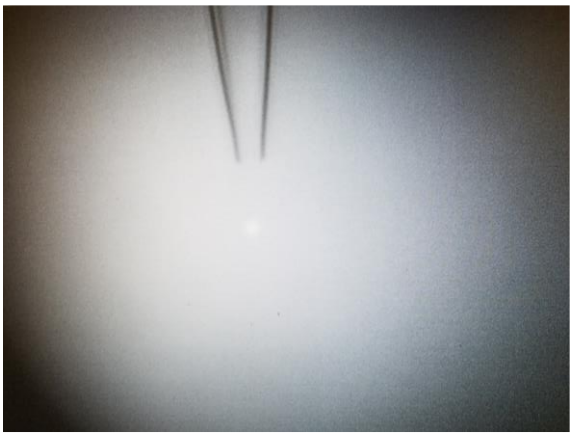

Figure 19: Image of the monitor displaying the micropipette tip and the spot of the laser trap.

By manually moving the flow-cell and the piezo stage, we can find the micropipette tip and bring it to a position relatively close to the laser trap (Figure 19).

We then finely align the counter propagating laser beams of the optical trap by following a sequence of adjustments. This involves manual alignment of the position sensing detectors (PSD) on either side and alignment of the objectives done with the piezo controller. We repeat this process by switching the view back and forth between the cameras on both sides until we see that the beams are overlapped indicated by the same image on both cameras.

Trapping Beads and Obtaining the Trap Stiffness

Once the basic laser alignment is done, streptavidin-coated polystyrene beads (Bangs Laboratories, CP01N) are added into the beads reservoir tube. Beads with mean diameter 4.95 µm were used initially and then switched to 3 µm (Spherotech, No. SVP-30-5) later on since they had better coating of streptavidin. Then the flow of beads into the flow-cell is turned on using the

flow control box until a bead is caught and held by the lasers. This bead is then fixated to the micropipette tip by suction.

A trap-stiffness test is done to assure that our optical trap is “stiff” enough by moving the bead attached to the tip across the optical trap and measuring light deflections to see whether the lasers are properly aligned (Figure 20). This is done by an automated program that controls the movement of the piezo stage holding the flow-cell and collects the deflection of the laser on the PSD. The axis marked as Force in the graph is essentially measuring the displacement of the laser recorded by the PSD, which is zero before the bead enters the trap and becomes zero after the bead completely traversed through the trap to the other side. The green and blue data in the graph represents two detectors on either side. The filled and open circles in the graph indicate the bead attached to the tip moving away and returning. If both lasers are properly aligned, the open circles will trace back the same curve as the tip returns back to the original position. The trap stiffness curve is saved to be used in the analysis program.

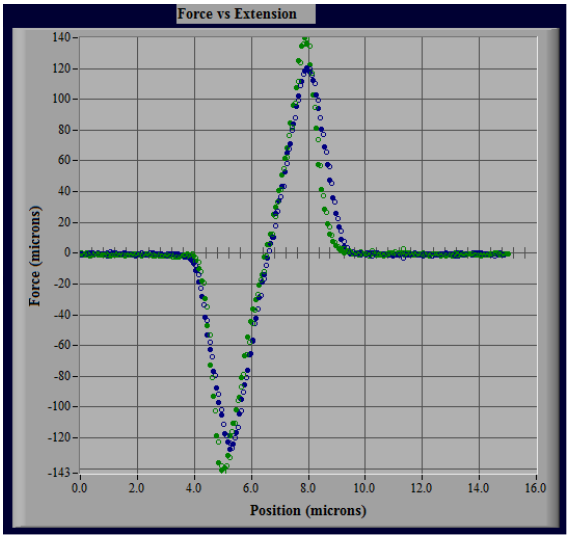

Figure 20: Image of a trap stiffness curve. The blue and green dots represent measured positions of the deflected beams by the PSDs.

Trapping a Single DNA Molecule

After obtaining the trap stiffness, we can progress towards trapping dsDNA molecules. A second bead is trapped with the lasers and the bead attached to the micropipette tip is brought in close proximity. The two beads are bumped against each other gently to ensure that they are in the same plane. Once we have these two beads, the excess beads are rinsed out by flowing buffer.

The biotinylated lambda dsDNA (labelled by Senior Research Scientist Dr. Micah McCauley at Williams Lab, Northeastern University) is added into the DNA reservoir tube and flowed into the flow-cell by turning on a very low pressure (<< 1 psi) onto the DNA-reservoir. The biotin, labelled on the dsDNA 3' ends, has a very high affinity to its complimentary chemical, streptavidin, which is coated on the beads. This results in a strong bond between the two, which can withstand high temperatures, pH, and forces, after coming in contact. During the flow, one end of a dsDNA gets chemically attached to the bead held by the lasers. Its other end is left hanging and floating along with the flow. We then will use the bead attached to the micropipette tip to fish around for that loosely floating end (we use the term fish because the dsDNA molecule is too small for us to see while we are trying to catch it, just how you can't see the fish until it is caught while fishing). Once the dsDNA molecule has been tethered in between the two beads, the bead in the trap will move when we move the bead attached to the tip. This movement is used to indicate that we have caught a DNA. A summary representing how we trap dsDNA and visualize the tether between the two beads is depicted in Figure 21[55].

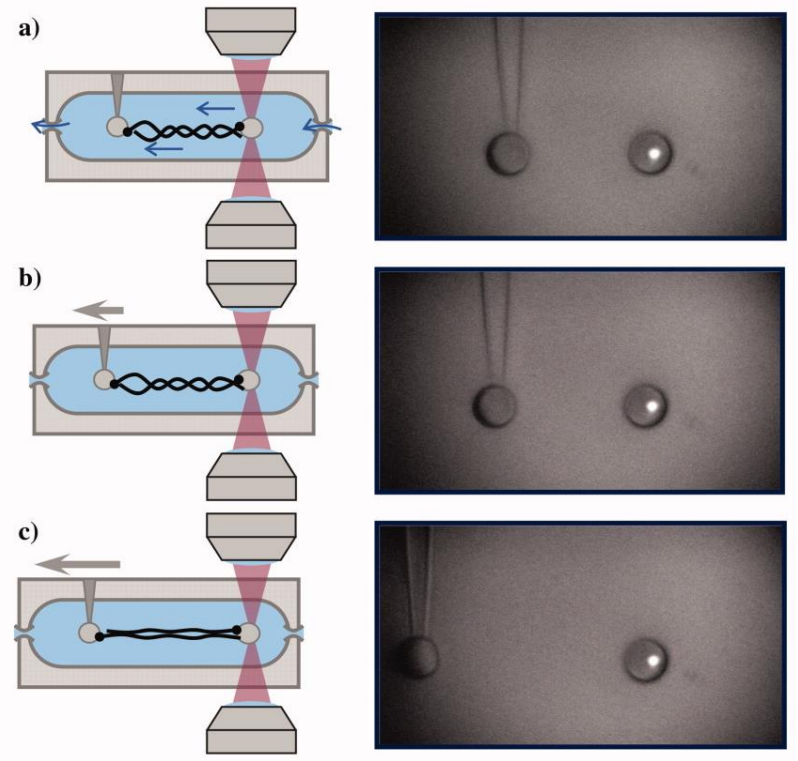

Figure 21: Schematic (left) and corresponding images seen during the experiments (right) of stretching a DNA molecule with optical tweezers at various stages. (a) DNA molecules are flowed into the flow-cell from the right side to left until one is caught between the two beads. (b) the DNA molecule is pulled towards the left causing it to stretch and (c) melt the double helix. In the images the micropipette tip, beads (~5 um) and the laser focus (~1 um, bright spot) are visible but the DNA is not. As the tip moves to the left, a tension is created in the DNA between the two beads, pulling the bead in the trap towards the left. (Adapted from Ref. 55)

Constant Force Measurements

After trapping the dsDNA molecule and washing out any excess dsDNA by flowing buffer, we can now manipulate and stretch it. Computer software is used to control the movement of the stage to take 100 nm steps and to measure the force exerted by recording the deflections of the laser in each detector. This produces a DNA stretching curve, which should resemble the characteristic curve previously mentioned in Figure 11. If it does not, it may be a result of having a damaged

dsDNA or multiple dsDNA caught between the beads. In this case the process of fishing for DNA is repeated.

Once a single DNA molecule is caught, the traditional experiments to study intercalators stretch and release dsDNA in the presence of intercalators at various concentrations. The binding kinetics of these molecules are fast enough to reach equilibrium during the stretch-release cycle. This allows us to apply thermodynamic and statistic models to characterize the interactions between the molecules and DNA.

As mentioned in the introduction, threading intercalators can take hours to reach their final binding form since they must thread their bulky ancillary ligands through the DNA base pairs. The time taken for typical dsDNA stretch-release curves are not sufficient for them to reach equilibrium. Therefore, to study our binuclear ruthenium complex, ΛΛ-P (synthesized by our collaborators from Chalmers University of Technology Sweden), we stretch and hold the dsDNA molecule at a certain force, to facilitate the threading process. The dsDNA is held at the constant force until the drug binding reaches its equilibrium using a force feedback loop created by the computer program. The elongation of the dsDNA as ΛΛ-P molecules bind to it is recorded as function of time by the program. These experiments are known as

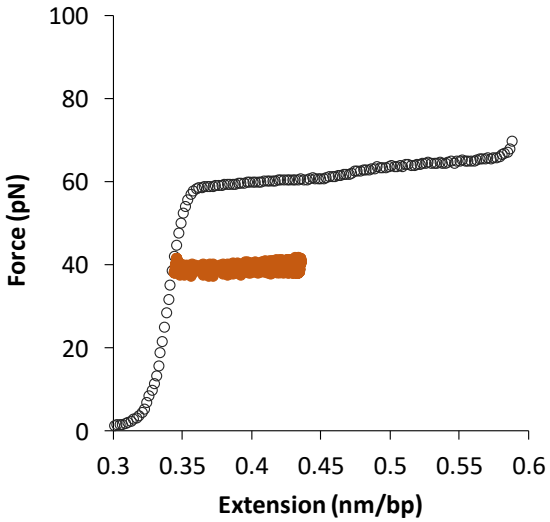

Figure 22: DNA stretching curve in the absence of drug (black open circles) and DNA extension obtained while holding at a constant force of 40 pN in the presence of 20nM concentration of ΛΛ-P (orange).

constant force measurements. Figure 22 shows an example from our data where a dsDNA molecule is held at a constant force of about 40 pN while flowing 20 nM ΛΛ-P. As ΛΛ-P binds, the DNA extends (orange) until reaching equilibrium.

Results

DNA Extension upon Binding to ΛΛ-P at a Constant Force

In the methods section, data from a force-extension curve for an example of a constant force measurement of ΛΛ-P binding dsDNA at 40 pN for 20 nM ΛΛ-P concentration was shown in Figure 22. That force-extension curve (Figure 23 left) is shown here along with the same extension data plotted as a function of time while we observe the dsDNA elongating until reaching a binding equilibrium (open circles in Figure 23 right).

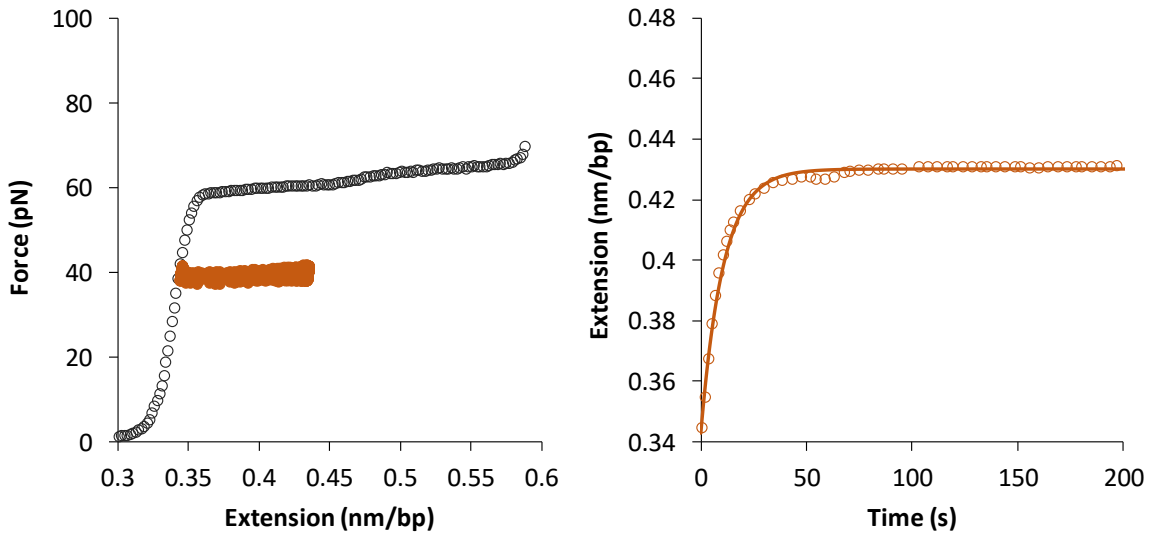

Figure 23: (Left) DNA stretching curve in the absence of drug (black open circles) and DNA extension obtained while holding at a constant force of 40 pN in the presence of 20nM concentration of ΛΛ-P (orange). (Right) DNA extension upon binding to ΛΛ-P as a function of time (open circles) and single exponential fit described by Equation 2 (solid line) at 40 pN and 20 nM ΛΛ-P.

The extension of dsDNA as ΛΛ-P binds as function of time can be described by a single exponential equation (solid line in Figure 23 right) of the form:

$$L(t) = L_0 + (L_{eq} - L_0)\left[1 - e^{-t/\left(\frac{1}{k_{fast}} + \frac{1}{k_{slow}}\right)}\right] \quad (2)$$

Where L_0 is the length of dsDNA in the absence of any ΛΛ-P bound complex, L_{eq} is the equilibrium lengthening that the extension reaches after ΛΛ-P binding reaches equilibrium, k_{fast} is the net fast rate, and k_{slow} is the net slow rate. The two rates indicate the binding occurs through two states, one relatively faster than the other (more details in the Discussion section). As we know the threading process is slow, here we are more interested in exploring the slow rate and going forward we will notate k_{slow} as k_{tot}, the net total rate of threading. This total net rate is a combination of both on and off rates, because while some molecules are binding to the DNA, some other molecules are coming off the DNA at the same time.

The theoretical fit for dsDNA extension were obtained by varying the parameters L_{eq}, k_{fast}, and k_{tot} to minimize the sum of chi-squares:

$$\chi^2 = \sum \left(\frac{L_{theoretical} - L_{experimental}}{\delta L}\right)^2 \quad (3)$$

Microsoft Excel's data analysis solver tool was used to return the best estimated values for those parameters. This fitting was done for each experimental data set collected.

This procedure was repeated for four different concentrations at 40 pN, and the results clearly show faster kinetics and higher equilibrium extension with increasing concentrations. Figure 24

shows representative data and fits at different concentrations obtained while holding the DNA at constant 40 pN force.

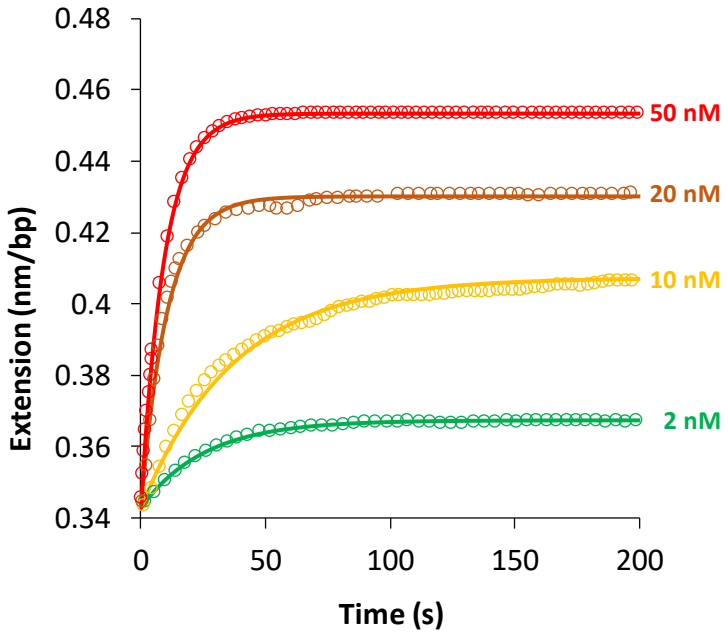

Figure 24: Representative data for DNA extensions as function of time in the presence of 2 nM (green), 10 nM (yellow), 20 nM (orange), and 50 nM (red) concentrations of ΛΛ-P at 40 pN. Open circles represent experimental data and solid lines represent best fit to Equation 2.

The average values obtained for L_{eq} are used in the forthcoming section to determine the binding affinity. The average values of k_{tot} obtained at various concentrations are later used in to determine the binding kinetics. We averaged at least three sets of data for each concentration in order to determine averages for L_{eq}, k_{fast}, and k_{tot} for each concentration.

Washing Away ΛΛ-P at a Constant Force

Our experiments also directly measured the dissociation rate, or how fast the molecules come off, by switching the flow of ΛΛ-P to buffer which allowed the molecules to wash off after reaching equilibrium. Open circles in Figure 25 show representative washing data obtained after reaching equilibrium with 4 different concentrations at 40 pN.

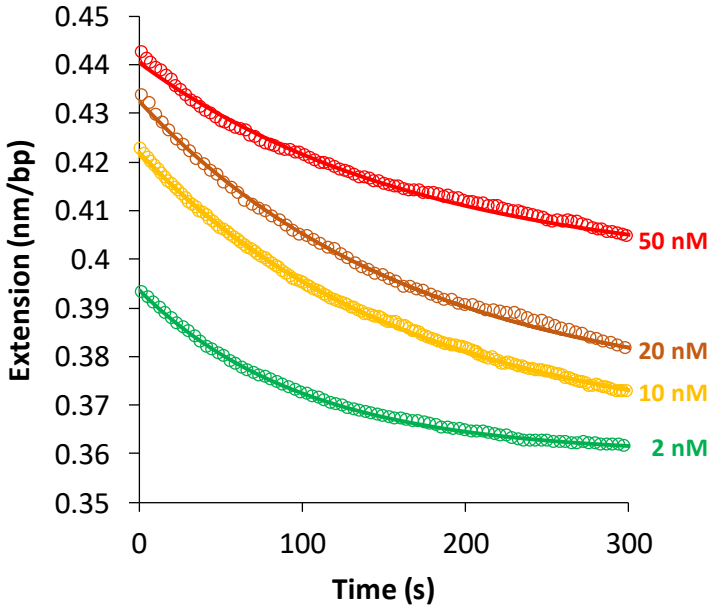

Figure 25: Representative data showing extension as function of time as ΛΛ-P is washed away by buffer after reaching equilibrium with 2 nM (green), 10 nM (yellow), 20 nM (orange), and 50 nM (red) concentrations of ΛΛ-P at 40 pN. Open circles represent experimental data and solid lines represent best fit to Equation 4.

The washing data can also be described by the single exponential expression:

$$L(t) = (L_{eq} - L_0)e^{-k_{off}t} + L_0 \quad (4)$$

Where k_{off} is the dissociation rate (L_0 and L_{eq} are the length of DNA in the absence of the drug and length of drug-DNA complex at equilibrium as previously defined in Equation 2). By following

the same analysis of averaging multiple data for each concentration, we can measure k_{off} at various concentrations at this force.

Binding Affinity & Dissociation Constant

Using the values for L_{eq} collected above at various concentrations C of $\Lambda\Lambda$-P at a particular force F, we can determine Θ, the experimental bound fraction of the drug:

$$\Theta(F, C) = \frac{\Delta L_{eq}}{\Delta L_{sat}} = \frac{L_{eq} - L_0}{L_{sat} - L_0} \tag{5}$$

Where ΔL_{eq} is the change in extension of the dsDNA to its equilibrium bound state and ΔL_{sat} is the change in extension of the dsDNA to its length obtained at saturated drug concentration, L_{sat}. Since fractional equilibrium binding values represent a fraction of base pairs with bound ligand at equilibrium, they are only assigned fractional values between 0 and 1. The fractional equilibrium binding values can be fit to the non-cooperative McGhee von Hippel (MGVH) Isotherm to determine a molecule's affinity, or potential binding strength between ligand and receptor, at a certain force:

$$\Theta(K_d, n) = \frac{C}{K_d}\left[\frac{n(1-\Theta)^n}{\left(1 - \Theta + \frac{\Theta}{n}\right)^{n-1}}\right] \tag{6}$$

Where K_d is the dissociation constant (the concentration at which the dsDNA is 50% saturated with the drug or inverse of binding strength), C is the concentration of the drug, and n is the binding site size. Using the reduced chi-squared analysis, we create theoretical values for Θ using Equation 5 and summing the squared differences between those theoretical values and our

experimental values. The sum is reduced while allowing ΔL_{sat}, K_d, and n to vary, thus returning the best fit and estimates for those values (Figure 26).

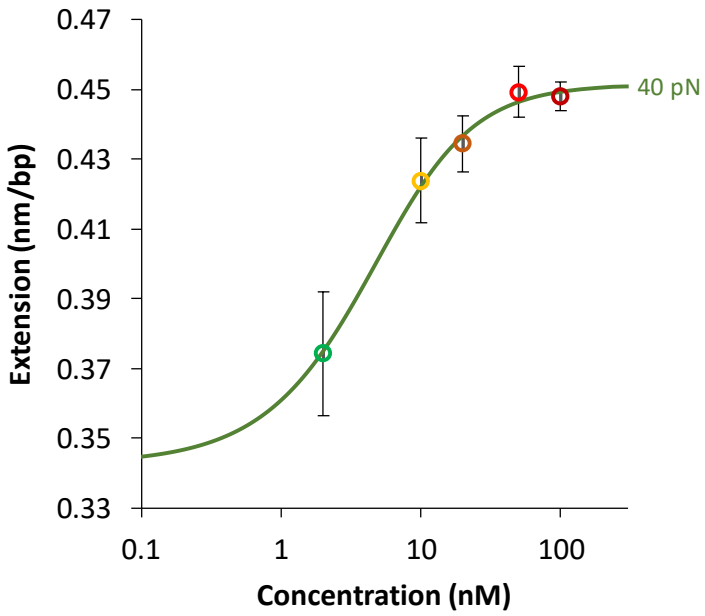

Figure 26: Experimental bound fractions best fitted to the MGVH isotherm at 40 pN. K_d estimated to be 4.97 ± 1.44 nM.

Force Dependent Binding Affinity

While we have been representing data for constant force measurements at 40 pN, we have studied various concentrations of $\Lambda\Lambda$-P at the constant forces of 20, 30, 40, and 50 pN (representative data for these forces are shown in Appendix A, data for 20 and 30 pN were collected by Nicholas Bryden '17)[60]. Using the MGVH analysis for all four forces (Figure 27) we can figure out the dissociation constant K_d at each force.

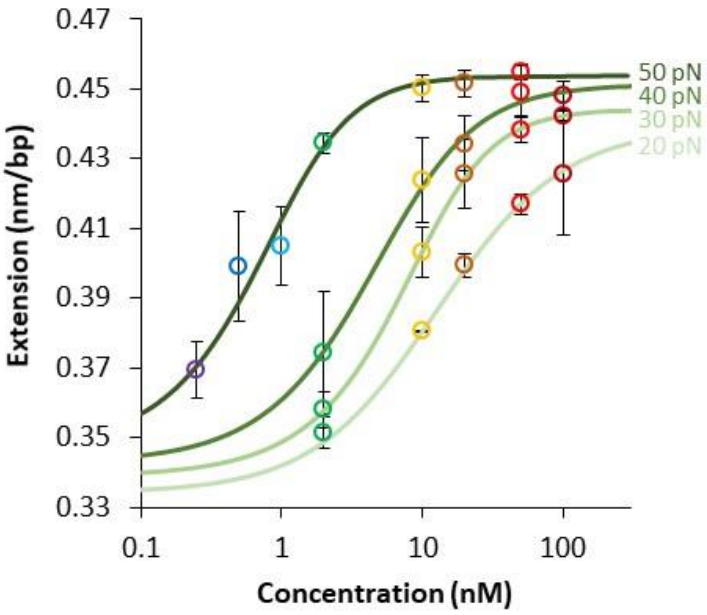

Figure 27: Experimental bound fractions of $\Lambda\Lambda$-P fit to the MGVH isotherm for 20, 30, 40, and 50 pN.

The values for K_d obtained at the four different forces is used to undergo a force dependent analysis to extrapolate the dissociation constant K_d in the absence of any force. It is shown from previous studies that the force (F) exponentially facilitates the binding by stretching the DNA and extending it by Δx, doing a work of $F\Delta x$. Allowing us to fit to the following exponential model:

$$K_d = K_d(0) exp\left(-\frac{F\Delta x_{eq}}{k_B T} \right) \quad (7)$$

Where $K_d(0)$ is the dissociation constant in the absence of any force, Δx_{eq} is the equilibrium elongation in the dsDNA for one intercalation event, k_B is Boltzmann constant, and T is the temperature in K (room temperature 294 K in our case).

The K_d values obtained at various forces (blue open circles) and the exponential force dependency (blue broken line) is shown on logarithmic scale plot in Figure 28. The y-intercept represents the binding affinity in the absence of force, $K_d(0) = 97 \pm 12$ nM. The lengthening of DNA upon a single intercalation event, $\Delta x_{eq} = 0.40 \pm 0.02$ nm, that we get is in par with other similar binuclear components studied (more to follow in the discussion section).

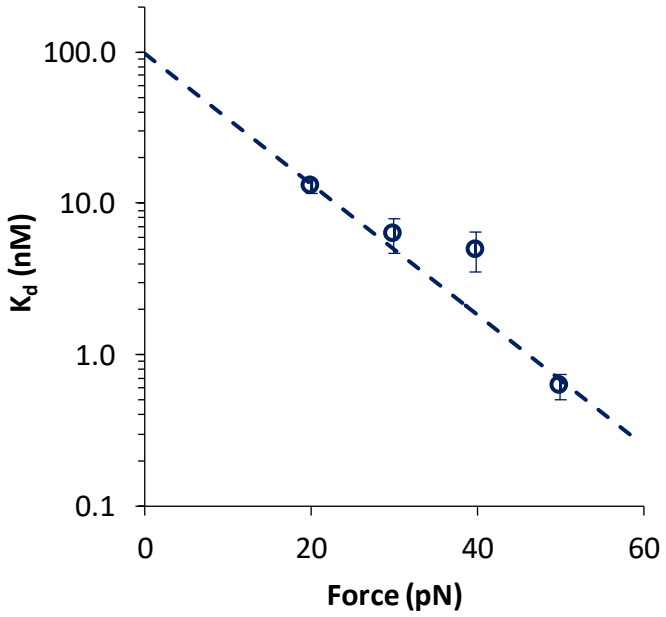

Figure 28: Force dependent analysis of Dissociation Constant K_d obtained from MGVH fits (open circles) and the fit to Equation 7 (broken line) yields $K_d(0) = 97 \pm 12$ nM and $\Delta x_{eq} = 0.40 \pm 0.02$ nm.

Binding Kinetics

As we mentioned earlier, the measured total rate of binding, k_{tot}, at a particular force and concentration can be defined as:

$$k_{tot} = k_{on} + k_{off} \tag{8}$$

Where k_{on} and k_{off} are the forward (on) and reverse (off) threading rates respectively.

Generally, the off rate, k_{off}, is independent of concentrations and on rate, k_{on}, is dependent on concentration, we can write the on rate as:

$$k_{on} = Ck_a \tag{9}$$

Where C is the drug concentration and k_a is the association constant. By substituting Equation 9 into Equation 8 for k_{on}, we get the following linear relationship between the total rate and concentration:

$$k_{tot} = Ck_a + k_{off} \tag{10}$$

Where the slope of the line is k_a and the y-intercept is k_{off}.

The total rates (k_{tot}) obtained by fitting our data obtained at 40 pN from fits in Figure 24 at various concentrations are shown as open circles in Figure 29 with the standard deviation as uncertainty.

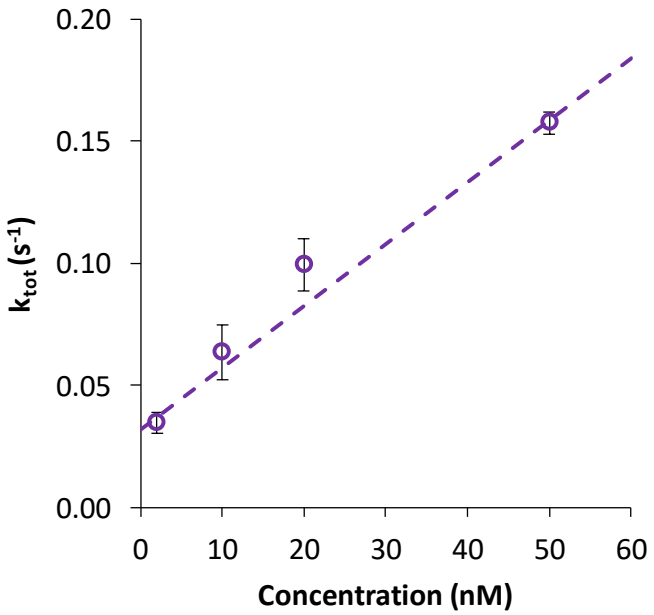

Figure 29: k_{tot} obtained with various concentrations of $\Lambda\Lambda$-P at 40 pN (open circles) fitted to the linear relationship expressed by Equation 10 (broken line) yields $k_a = (25.3 \pm 1.3) \times 10^5\ M^{-1}s^{-1}$ and $k_{off} = 0.031 \pm 0.004\ s^{-1}$.

This is fit to Equation 10 by minimizing the sum of chi-square to estimate k_a and k_{off}. The broken line in Figure 28 shows the best fit to Equation 10 yielding us $k_a = (25.3 \pm 1.3) \times 10^5$ $M^{-1}s^{-1}$ and $k_{off} = 0.031 \pm 0.004$ s^{-1} at 40 pN. This analysis was done for each constant force data to obtain k_a and k_{off} at each force.

Association Rate as a Function of Force

The binding kinetics analysis explained in the previous section yielded association constant k_a for all four forces studied. This data is represented as open circles in Figure 30 with standard deviation as the uncertainty.

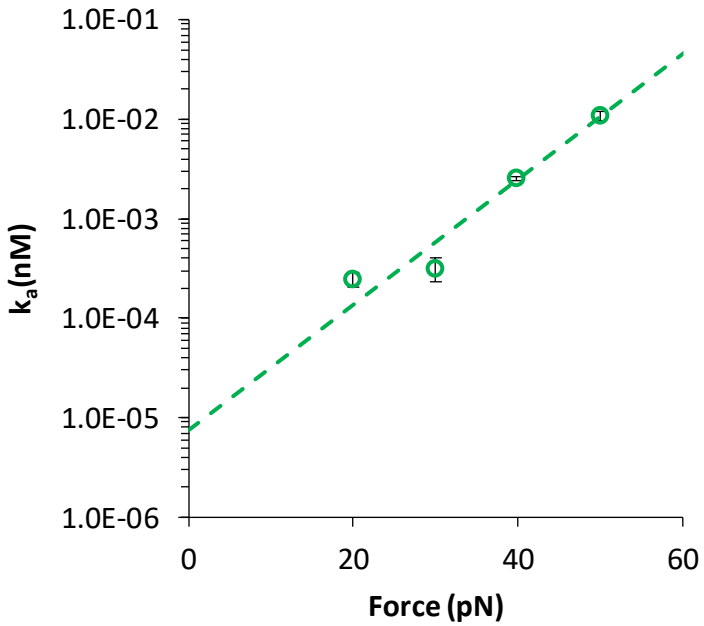

Figure 30: Force dependent analysis of k_a. The association rates obtained at various force (open circles) with uncertainty (standard deviation) fitted to Equation 11.
The fit yields $k_a(0) = (7.5 \pm 0.2) \times 10^3 M^{-1}s^{-1}$ and $x_{on} = 0.54 \pm 0.03$ nm.

We undergo a similar force dependent analysis as we did earlier to extrapolate the association rate $k_a(0)$ in the absence of force. Here we use the exponential relation:

$$k_a = k_a(0)exp\left(\frac{Fx_{on}}{k_BT}\right) \quad (11)$$

Where $k_a(0)$ is the association constant in the absence of any force and x_{on} is the dsDNA elongation required for the association of one ligand.

By minimizing the sum of chi-squares, the data is fit according to Equation 11 (broken line in figure 30). The fit yields $k_a(0) = (7.5 \pm 0.2) \times 10^3$ $M^{-1}s^{-1}$ as our association constant for $\Lambda\Lambda$-P in the absence of force and the elongation required to thread a single molecule as $x_{on} = 0.54 \pm 0.03$ nm.

Unthreading Rate as a Function of Force

Using averaged k_{off} values for various concentration measured directly from the washing data (Figure 25), we determine the average k_{off} at 40 pN force. This was done for the other forces studied to determine k_{off} for $\Lambda\Lambda$-P at 20, 30, and 50 pN.

From the wash analysis for all four forces combined, we undergo a force dependent analysis to extrapolate the off rate k_{off} in the absence of any force. Using a similar exponential relation assuming the force facilitates the unthreading process we get:

$$k_{off} = k_{off}(0)exp\left(\frac{Fx_{off}}{k_BT}\right) \quad (12)$$

Where $k_{off}(0)$ is the off rate in the absence of force and x_{off} is the dsDNA elongation required for the unthreading of one ligand.

The k_{off} averages obtained from washing off experiments (open circles in Figure 31) were fit to Equation 12 by minimizing the sum of chi-squares. The fit yields our off rate for $\Lambda\Lambda$-P in the absence of force, $k_{off}(0) = (3.4 \pm 0.7) \times 10^{-3}\text{s}^{-1}$ and the lengthening required to unthread $x_{off} = 0.09 \pm 0.02$ nm.

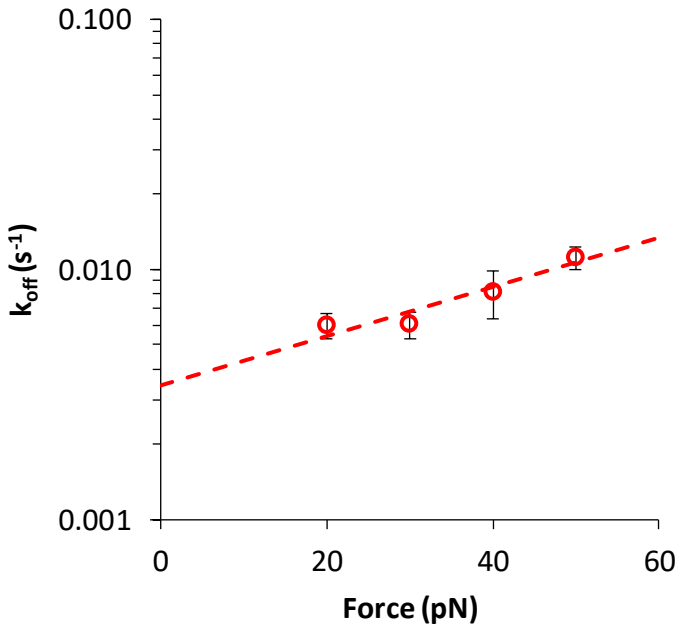

Figure 31: Force dependent analysis of k_{off}. The off rates obtained from washing experiments (open circles) fitted to Equation 12 (broken line) yields $k_{off}(0) = (3.4 \pm 0.7) \times 10^{-3}s^{-1}$ and $x_{off} = 0.09 \pm 0.02$ nm.

Discussion

Why Two-State Binding Model of ΛΛ-P?

Before following the two-state model kinetic analysis shown in the results section, we had initially used the traditional exponential equation with a single rate:

$$L(t) = L_0 + (L_{eq} - L_0)(1 - e^{-k_{tot}t}) \quad (13)$$

Where the only rate k_{tot} describes the net rate of binding, to fit the extensions of dsDNA as ΛΛ-P binds as function of time. Although the fits looked reasonable from the single state analysis (Appendix B), the complete analysis done with this model having only one net rate led to physically unreliable solutions. The estimated structural changes required to bind the drug from this analysis required DNA to lengthen almost 3 times the base separation, which is not physically feasible. This kinetic analysis also ended up with an extremely high dissociation constant, over two orders of magnitude that is obtained from the MGVH analysis. Furthermore, the structural changes of the dsDNA from ΛΛ-P binding obtained from this kinetic analysis ($x_{off} = 0.00 \pm 0.03$ nm and $\Delta x_{eq} = 0.79 \pm 0.01$ nm) did not agree with value obtained from washing experiments directly ($x_{off} = 0.09 \pm 0.02$ nm) and MGVH analysis ($\Delta x_{eq} = 0.40 \pm 0.02$ nm).

On the contrary, $x_{off} = 0.08 \pm 0.02$ nm and $\Delta x_{eq} = 0.45 \pm 0.03$ nm obtained from the kinetic analysis of two-state model agree reasonably well within the uncertainty with the results obtained from washing and MGVH model fitting. The K_d obtained from two-state kinetics is in the same order of magnitude as the one obtained from MGVH analysis. The extension required by dsDNA

to thread one ΛΛ-P molecule, x_{on}, also yields a reasonable value. The table in Appendix C shows the comparison between the two analysis. The results tabulated explain clearly why we chose the two-state binding model.

Our suggestion is that the binding occurs in a two-state system, initially binding very fast to the dsDNA grooves and then slowly threading between the base pairs. This two-state binding was observed by our collaborators for many ruthenium binuclear molecules in linear dichroism experiments[32] (Figure 32) but was not detected in single molecule experiments with other binuclear molecules that have been studied so far[37,38]. We represent the rate of this process by Equation 2 to isolate the slow rate (k_{slow}) which we assume as the net threading rate (k_{tot}). Although k_{fast} is not used is our analysis, our data suggests that the k_{fast} values vary slightly with increasing concentration and are force dependent.

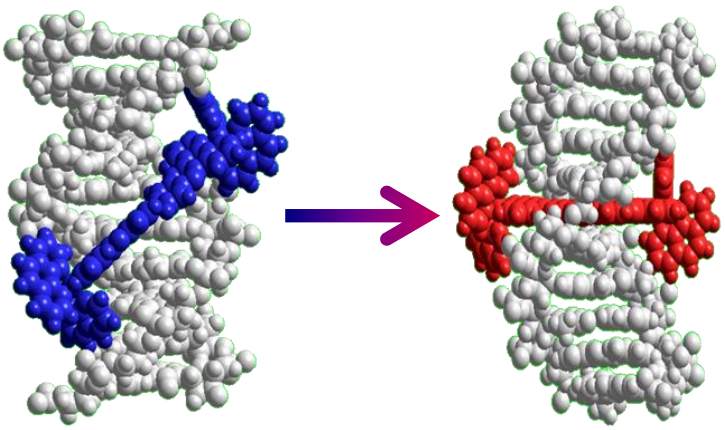

Figure 32: Two-state binding of a binuclear ruthenium complex predicted by linear dichroism experiments. Initially the complex binds very fast to the dsDNA grooves (blue) before finally reaching the threading intercalation state (red).
(Figure adapted from Ref. 32)

Chirality Effects on Binding Properties of Threading Intercalation

The results quantifying ΛΛ-P binding strength, kinetics, and structural changes that DNA undergo while binding to a single molecule are tabulated against the previously studied molecule with the same chemical structure but opposite chirality (ΔΔ-P) in Table 1.

Table 1: Comparison of the binding properties and kinetics of ΛΛ-P and ΔΔ-P.

Binding Properties	ΛΛ-P	ΔΔ-P[†]
$K_d(0)$	97 ± 12 nM	44 ± 2 nM
$k_a(0)$	(7.5 ± 0.2) x10^3 $M^{-1}s^{-1}$	(10.1 ± 0.1) x10^3 $M^{-1}s^{-1}$
$k_{off}(0)$	(3.4 ± 0.7) x10^{-3} s^{-1}	(1.4 ± 0.1) x10^{-3} s^{-1}
Δx_{eq}	0.40 ± 0.02 nm	0.19 ± 0.01 nm
x_{on}	0.54 ± 0.03 nm	0.33 ± 0.01 nm
x_{off}	0.09 ± 0.02 nm	0.14 ± 0.01 nm

[†]Almaqwashi, A. A. et al. Strong DNA deformation required for extremely slow DNA threading intercalation by a binuclear ruthenium complex. Nucleic Acids Res 42, 11634-11641 (2014).

**Appendix D provides a comparison between these chiral molecules and a similar binuclear ruthenium molecule (ΔΔ-B) with the same intercalating moiety but smaller ancillary ligands.*

The dsDNA threading by ΛΛ-P has been shown to be strongly dependent on force, indicated by the exponential decrease of the dissociation constant K_d with increasing force (Figure 28), just as ΔΔ-P demonstrated. Although ΛΛ-P molecules exhibit a slightly higher value for K_d compared to ΔΔ-P, they are within the same order of magnitude, which can be explained as a result of their common intercalating dppz moieties.

Threading into dsDNA, we measured the association rate k_a of ΛΛ-P to be slightly slower than that of its previously studied enantiomer ΔΔ-P. This also had been observed in bulk assay studies. This can be explained by the larger structural changes required by the ΛΛ-P to thread discussed below.

The DNA elongation required for the threading of each ΛΛ-P ligand, x_{on} (0.54 ± 0.01 nm), is much larger than for ΔΔ-P (0.33 ± 0.01 nm). Once the bulky ancillary ligands thread and the threading dppz moiety of molecule is settled between the DNA base pairs this length shrinks back to an

equilibrium length (Δx_{eq}). The equilibrium elongation of the dsDNA for each intercalation event, is almost double for ΛΛ-P (0.40 ± 0.02 nm) compared to ΔΔ-P (0.19 ± 0.01 nm). This may be an effect of the opposing chirality of the left-handed ancillary ligands of complex ΛΛ-P not fitting well in right-handed dsDNA due to steric hindrance. The DNA elongation required for the unthreading of each ΛΛ-P ligand, x_{off} (0.09 ± 0.02 nm), indicates that you have to elongate the base pairs by 0.09 nm further than it's equilibrium to unthread ΛΛ-P, which is less than the elongation required for ΔΔ-P (0.14 ± 0.01 nm). This explains the slightly faster off rates obtained for ΛΛ-P compared to ΔΔ-P. These structural changes suggest a locking mechanism in both molecules as depicted by Figure 33.

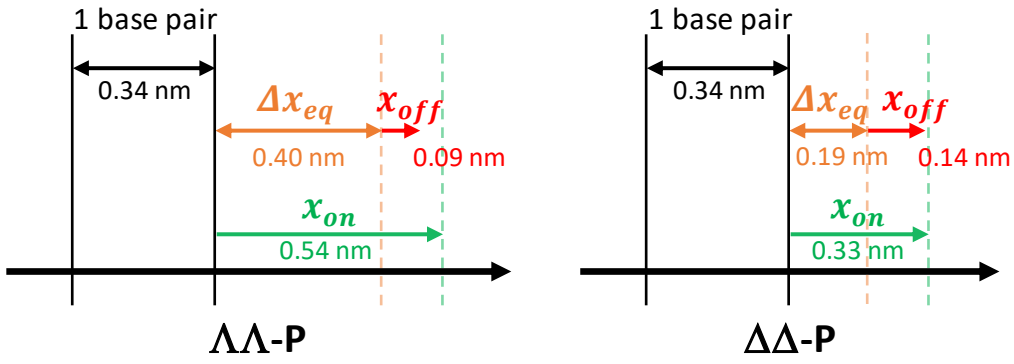

Figure 33: Illustration highlighting the locking mechanism based on the structural changes dsDNA undergoes as ΛΛ-P (left) and ΔΔ-P (right) bind through threading intercalation.

Our studies suggest that left-handed molecules bind less favorably to DNA with slower binding kinetics and lower binding affinity, and it is explained by the structural changes that occur at the molecular level of the threading.

Appendix A: Representative Data from Two State Analysis

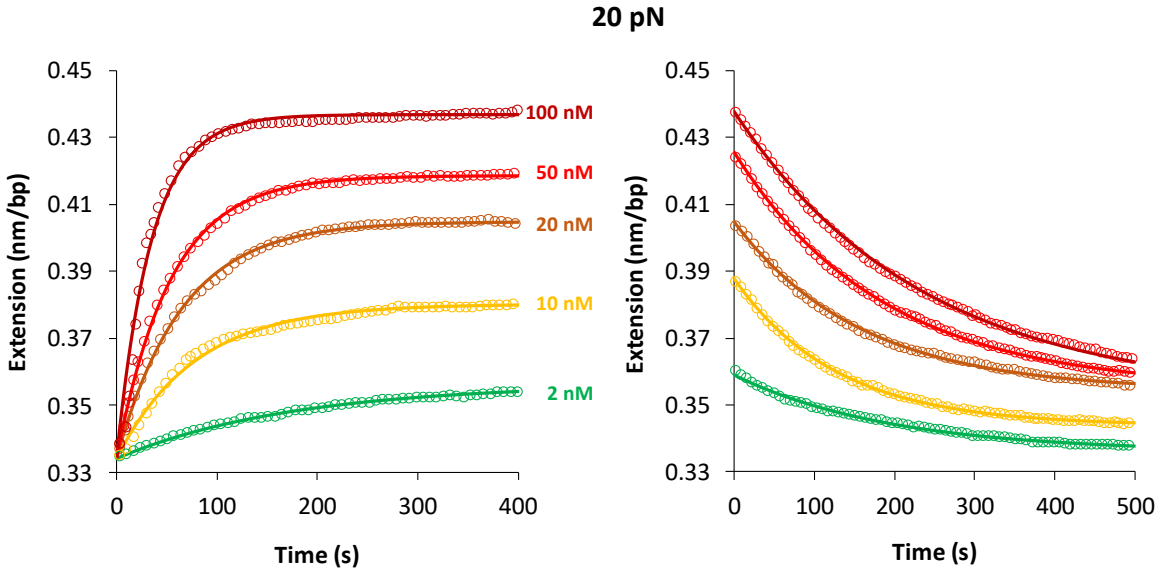

Figure B1: Representative data for DNA extensions as function of time for various ΛΛ-P concentrations at 20 pN force (left). Open circles represent experimental data and solid lines represent best fit to the two state analysis according Equation 2. Corresponding data showing extensions as function of time as ΛΛ-P is washed away by buffer after reaching equilibrium (right). Open circles represent experimental data and solid lines represent best fit to Equation 4.

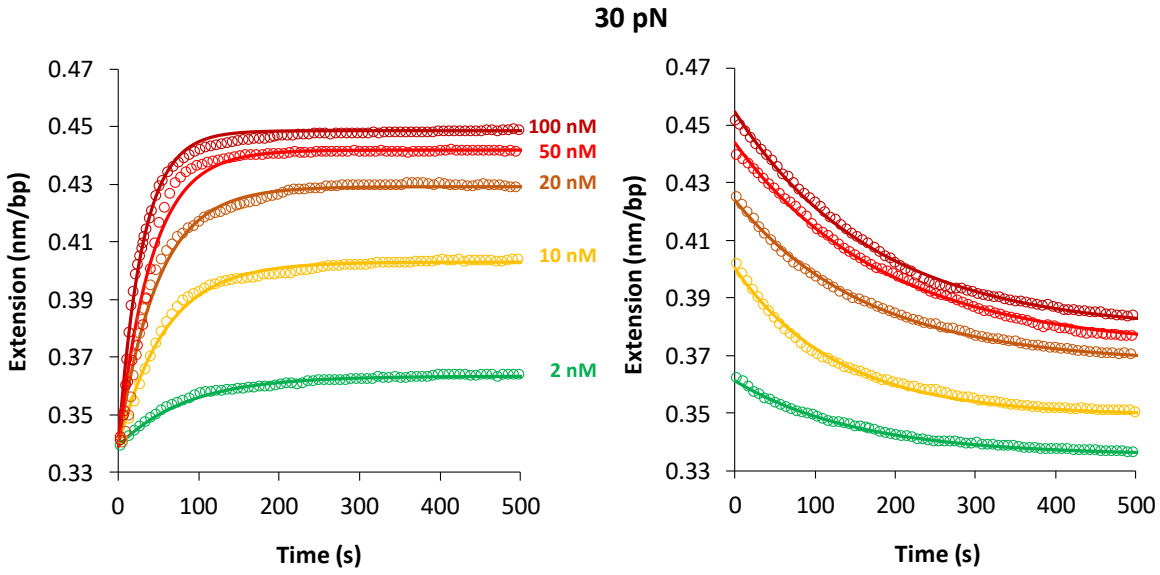

Figure B2: Representative data for DNA extensions as function of time for various ΛΛ-P concentrations at 30 pN force (left). Open circles represent experimental data and solid lines represent best fit to the two state analysis according Equation 2. Corresponding data showing extensions as function of time as ΛΛ-P is washed away by buffer after reaching equilibrium (right). Open circles represent experimental data and solid lines represent best fit to Equation 4.

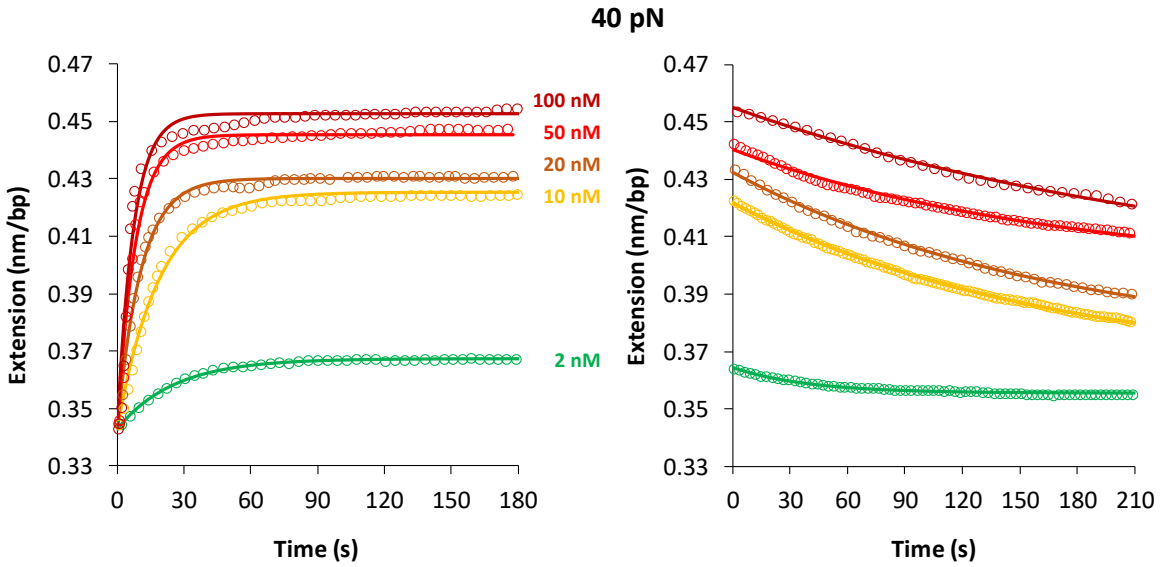

Figure B3: Representative data for DNA extensions as function of time for various $\Lambda\Lambda$-P concentrations at 40 pN force (left). Open circles represent experimental data and solid lines represent best fit to the two state analysis according Equation 2. Corresponding data showing extensions as function of time as $\Lambda\Lambda$-P is washed away by buffer after reaching equilibrium (right). Open circles represent experimental data and solid lines represent best fit to Equation 4.

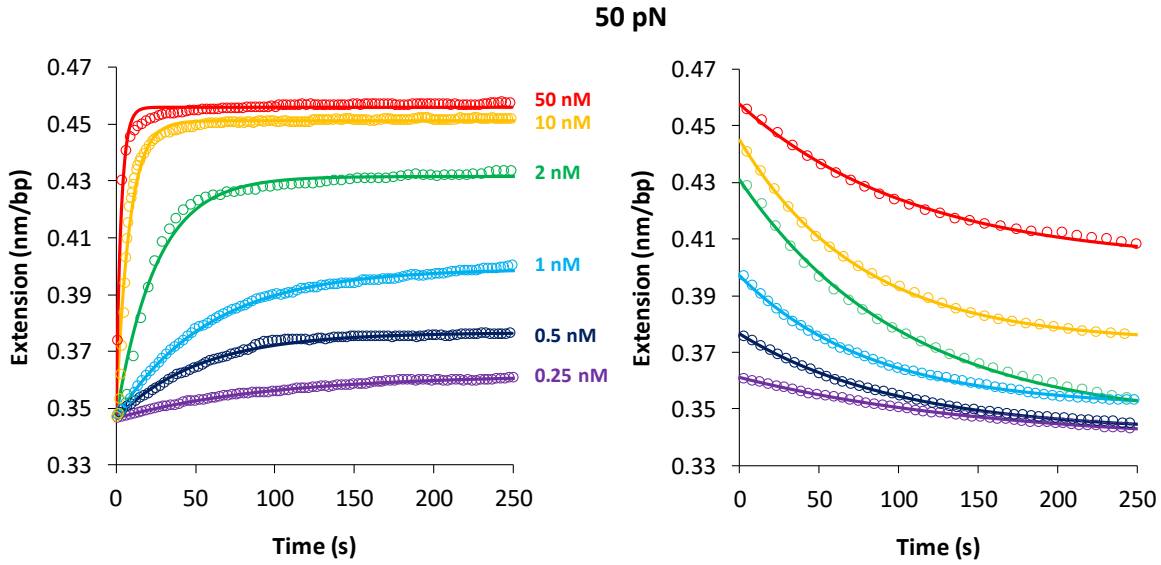

Figure B4: Representative data for DNA extensions as function of time for various $\Lambda\Lambda$-P concentrations at 40 pN force (left). Open circles represent experimental data and solid lines represent best fit to the two state analysis according Equation 2. Corresponding data showing extensions as function of time as $\Lambda\Lambda$-P is washed away by buffer after reaching equilibrium (right). Open circles represent experimental data and solid lines represent best fit to Equation 4.

Appendix B: Representative Data from Single State Analysis

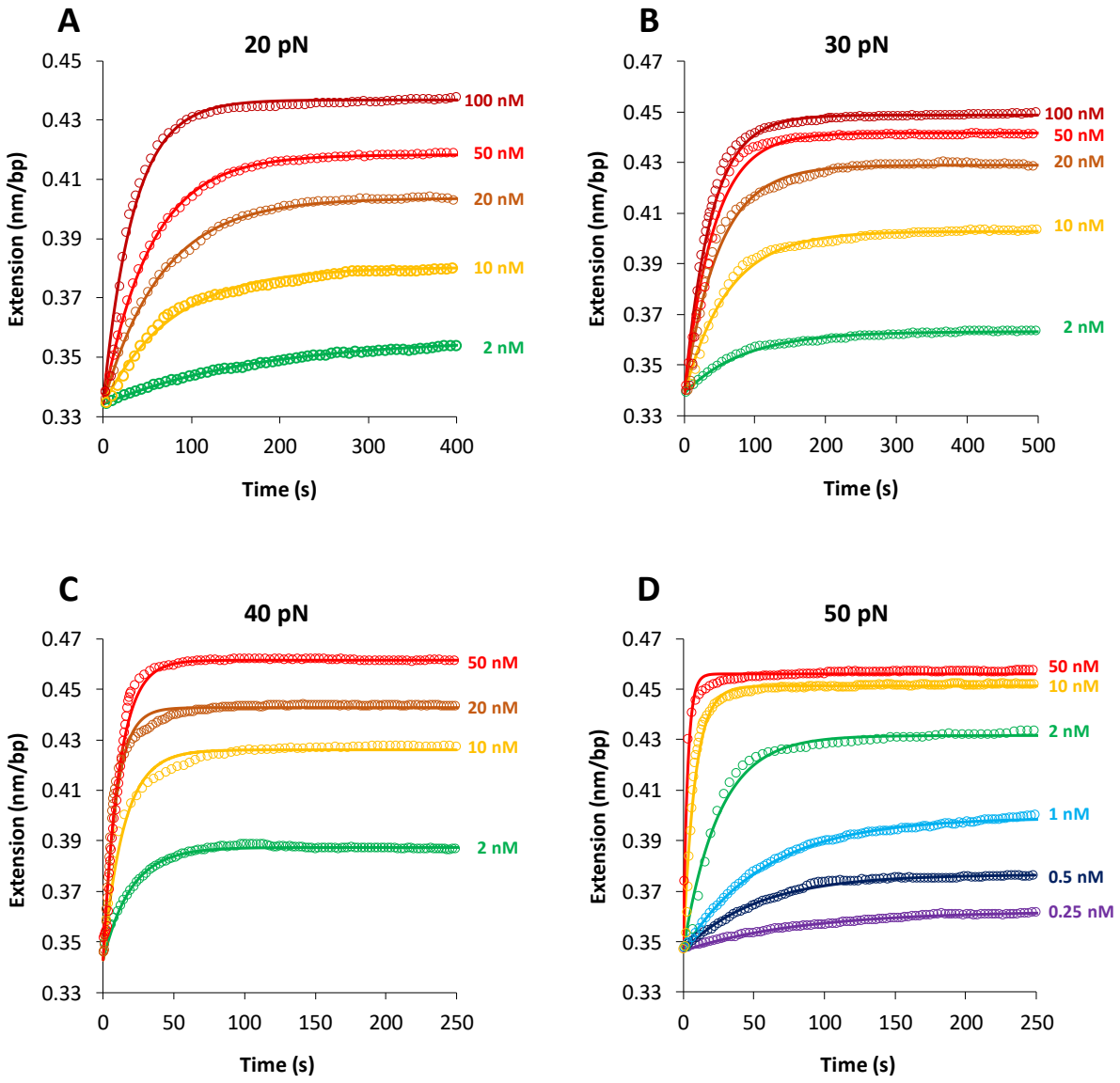

Figure A1: Representative data for DNA extensions as function of time for various $\Lambda\Lambda$-P concentrations at the 20 (A), 30 (B), 40 (C), and 50 (D) pN forces. Open circles represent experimental data and solid lines represent best fit to the single state analysis according Equation 13.

Appendix C: Comparing Single and Two State Analysis Data

Table C1: Comparison of the binding properties and kinetics of $\Lambda\Lambda$-P in single state and two state analysis.

Binding Properties	Single State	Two State
K_d(0) from MGVH	97 ± 12 nM	97 ± 12 nM
K_d(0) from Kinetics	7833 ± 2431 nM	638 ± 263 nM
K_d(0) from k_{off}/k_a	5954 nM	452 nM
k_a(0)	571 ± 48 $M^{-1}s^{-1}$	7500 ± 200 $M^{-1}s^{-1}$
k_{off}(0) from k_{tot}	0.0148 ± 0.0009 s^{-1}	0.0098 ± 0.0016 s^{-1}
k_{off}(0) from Wash	0.0034 ± 0.0007 s^{-1}	0.0034 ± 0.0007 s^{-1}
Δx_{eq} from MGVH	0.40 ± 0.02 nm	0.40 ± 0.02 nm
Δx_{eq} from Kinetics	0.79 ± 0.01 nm	0.45 ± 0.03 nm
x_{on}	0.79 ± 0.01 nm	0.54 ± 0.03 nm
x_{off} from Kinetics	0.00 ± 0.03 nm	0.08 ± 0.02 nm
x_{off} from Wash	0.09 ± 0.02 nm	0.09 ± 0.02 nm

Appendix D: Comparing the Binding with Different Sized Ancillary Ligands

Table D1: Comparison of the binding properties and kinetics of ΛΛ-P, ΔΔ-P, and ΔΔ-B.

Binding Properties	ΛΛ-P	ΔΔ-P[†]	ΔΔ-B[ǂ]
$K_d(0)$	97 ± 12 nM	44 ± 2 nM	65 ± 5 nM
$k_a(0)$	(7.5 ± 0.2) x10^3 $M^{-1}s^{-1}$	(10.1 ± 0.1) x10^3 $M^{-1}s^{-1}$	(121 ± 12) x10^3 $M^{-1}s^{-1}$
$k_{off}(0)$	(3.4 ± 0.7) x10^{-3} s^{-1}	(1.4 ± 0.1) x10^{-3} s^{-1}	(7.1 ± 0.6) x10^3 s^{-1}
Δx_{eq}	0.40 ± 0.02 nm	0.19 ± 0.01 nm	0.28 ± 0.02 nm
x_{on}	0.54 ± 0.03 nm	0.33 ± 0.01 nm	0.26 ± 0.01 nm
x_{off}	0.09 ± 0.02 nm	0.14 ± 0.01 nm	-0.02 ± 0.01 nm

[†]*Almaqwashi, A. A. et al. Strong DNA deformation required for extremely slow DNA threading intercalation by a binuclear ruthenium complex. Nucleic Acids Res 42, 11634-11641 (2014).*

[ǂ]*Clark, A. G. et al. Reshaping the Energy Landscape Transforms the Mechanism and Binding Kinetics of DNA Threading Intercalation. Biochemistry 57, 614-619 (2018).*

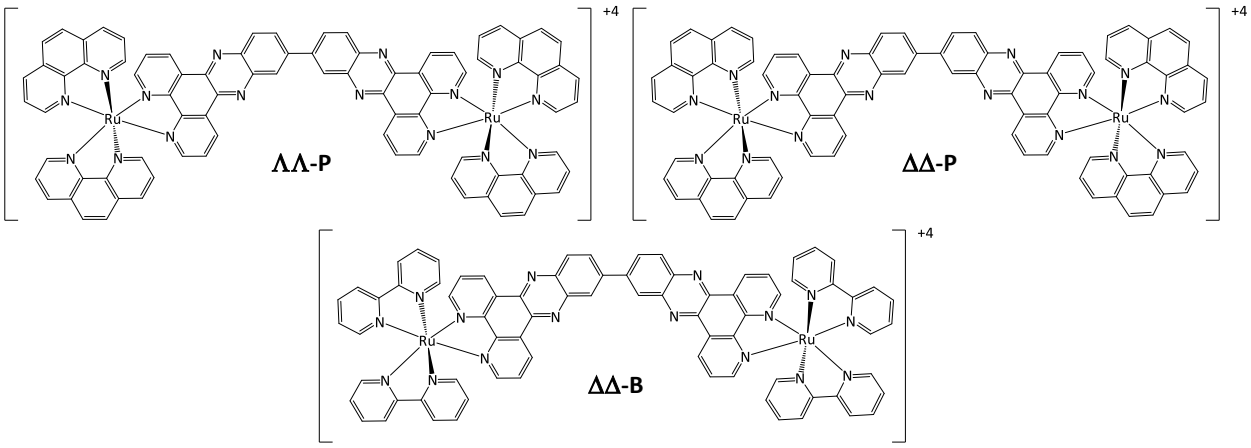

Figure D1: Chemical structures of ΛΛ-[μ-bidppz(phen)$_4$Ru2]$^{4+}$ (ΛΛ-P), ΔΔ-[μ-bidppz(phen)$_4$Ru2]$^{4+}$ (ΔΔ-P), and ΔΔ-[μ-bidppz(bpy)$_4$Ru$_2$]$^{4+}$ (ΔΔ-B). ΛΛ-P and ΔΔ-P differ only by chirality, whereas ΔΔ-B differs by its ancillary ligands, bipyridine (bpy), compared to phenanthroline (phen) in ΛΛ-P and ΔΔ-P. The dark wedges linked from the Ru atoms indicate that the ancillary ligand is pointed out of the page, whereas the dashed wedges indicate that the ancillary ligand is pointed into the page.

References

1 *Glossary: Definitions & Phonetic Pronunciations*, <https://www.cancer.org/cancer/glossary.html#alpha-c> (2020).

2 Reece, J. B. *et al. Campbell biology*. (Pearson Boston, MA, 2014).

3 Liu, M. *et al.* Sensitive and specific multi-cancer detection and localization using methylation signatures in cell-free DNA. *Annals of Oncology* (2020).

4 *A blood test finds deadly cancers before symptoms start*, <https://www.nature.com/articles/d41586-020-00959-9> (2020).

5 *The Genetics of Cancer*, <https://www.cancer.gov/about-cancer/causes-prevention/genetics> (2017).

6 Mendel, G. Experiments in plant hybridization (1865). *Verhandlungen des naturforschenden Vereins Brünn) Available online* (1996).

7 Dahm, R. Discovering DNA: Friedrich Miescher and the early years of nucleic acid research. *Hum Genet* **122**, 565-581 (2008).

8 Griffith, F. The significance of pneumococcal types. *Epidemiology & Infection* **27**, 113-159 (1928).

9 Avery, O. T., MacLeod, C. M. & McCarty, M. Studies on the chemical nature of the substance inducing transformation of pneumococcal types: induction of transformation by a desoxyribonucleic acid fraction isolated from pneumococcus type III. *The Journal of experimental medicine* **79**, 137-158 (1944).

10 Levene, P. The structure of yeast nucleic acid. *Studies from the Rockefeller Institute for Medical Research* **30**, 221 (1919).

11 Chargaff, E., Lipshitz, R., Green, C. & Hodes, M. The composition of the desoxyribonucleic acid of salmon sperm. *Journal of Biological Chemistry* **192**, 223-230 (1951).

12 Watson, J. D. & Crick, F. H. Molecular structure of nucleic acids: A structure for deoxyribose nucleic acid. *Nature* **171**, 3.12 (1953).

13 Franklin, R. E. & Gosling, R. G. Evidence for 2-chain helix in crystalline structure of sodium deoxyribonucleate. *Nature* **172**, 156-157 (1953).

14 Pray, L. Discovery of DNA structure and function: Watson and Crick. *Nature Education* **1**, 100 (2008).

15 Chaurasiya, K. R., Paramanathan, T., McCauley, M. J. & Williams, M. C. Biophysical characterization of DNA binding from single molecule force measurements. *Phys Life Rev* **7**, 299-341 (2010).

16 Lerman, L. Structural considerations in the interaction of DNA and acridines. *Journal of molecular biology* **3**, 18-IN14 (1961).

17 Smith, B. *Synthetic Receptors for Biomolecules: Design Principles and Applications*. (2015).

18 McCauley, M. J. & Williams, M. C. Optical tweezers experiments resolve distinct modes of DNA-protein binding. *Biopolymers: Original Research on Biomolecules* **91**, 265-282 (2009).

19 Lian, C., Robinson, H. & Wang, A. H.-J. Structure of actinomycin D bound with (GAAGCTTC) 2 and (GATGCTTC) 2 and its binding to the (CAG) n:(CTG) n triplet sequence as determined by NMR analysis. *Journal of the American Chemical Society* **118**, 8791-8801 (1996).

20 Waring, M. J. DNA modification and cancer. *Annual review of biochemistry* **50**, 159-192 (1981).

21 Paramanathan, T. *et al.* Mechanically manipulating the DNA threading intercalation rate. *J Am Chem Soc* **130**, 3752-3753 (2008).

22 Williams, L. D. *et al.* Structure of nogalamycin bound to a DNA hexamer. *Proceedings of the National Academy of Sciences* **87**, 2225-2229 (1990).

23 Arora, S. Molecular structure, absolute stereochemistry, and interactions of nogalamycin, a DNA-binding anthracycline antitumor antibiotic. *Journal of the American Chemical Society* **105**, 1328-1332 (1983).
24 Rosenberg, B., Van Camp, L. & Krigas, T. Inhibition of cell division in Escherichia coli by electrolysis products from a platinum electrode. *Nature* **205**, 698-699 (1965).
25 Murry, D. J. Comparative clinical pharmacology of cisplatin and carboplatin. *Pharmacotherapy: The Journal of Human Pharmacology and Drug Therapy* **17**, 140S-145S (1997).
26 Barton, J. K., Danishefsky, A. & Goldberg, J. Tris (phenanthroline) ruthenium (II): stereoselectivity in binding to DNA. *Journal of the American Chemical Society* **106**, 2172-2176 (1984).
27 Hartinger, C. G. *et al.* From bench to bedside–preclinical and early clinical development of the anticancer agent indazolium trans-[tetrachlorobis (1H-indazole) ruthenate (III)](KP1019 or FFC14A). *Journal of inorganic biochemistry* **100**, 891-904 (2006).
28 Sava, G., Alessio, E., Bergamo, A. & Mestroni, G. in *Metallopharmaceuticals I* 143-169 (Springer, 1999).
29 Mihailovic, A. *et al.* Exploring the interaction of ruthenium (II) polypyridyl complexes with DNA using single-molecule techniques. *Langmuir* **22**, 4699-4709 (2006).
30 Vladescu, I. D., McCauley, M. J., Nunez, M. E., Rouzina, I. & Williams, M. C. Quantifying force-dependent and zero-force DNA intercalation by single-molecule stretching. *Nat Methods* **4**, 517-522 (2007).
31 Haq, I. *et al.* Interaction of. delta.-and. lambda.-[Ru (phen) 2DPPZ] 2+ with DNA: a calorimetric and equilibrium binding study. *Journal of the American Chemical Society* **117**, 4788-4796 (1995).
32 Wilhelmsson, L. M., Westerlund, F., Lincoln, P. & Nordén, B. DNA-Binding of Semirigid Binuclear Ruthenium Complex Δ, Δ-[μ-(11, 11 '-bidppz)(phen) 4Ru2] 4+: Extremely Slow Intercalation Kinetics. *Journal of the American Chemical Society* **124**, 12092-12093 (2002).
33 Lincoln, P. & Nordén, B. Binuclear ruthenium (II) phenanthroline compounds with extreme binding affinity for DNA. *Chemical Communications*, 2145-2146 (1996).
34 Wilhelmsson, L. M., Esbjörner, E. K., Westerlund, F., Nordén, B. & Lincoln, P. Meso Stereoisomer as a Probe of Enantioselective Threading Intercalation of Semirigid Ruthenium Complex [μ-(11, 11 '-bidppz)(phen) 4Ru2] 4+. *The Journal of Physical Chemistry B* **107**, 11784-11793 (2003).
35 Westerlund, F., Eng, M. P., Winters, M. U. & Lincoln, P. Binding geometry and photophysical properties of DNA-threading binuclear ruthenium complexes. *The Journal of Physical Chemistry B* **111**, 310-317 (2007).
36 Müller, W. & Crothers, D. M. Studies of the binding of actinomycin and related compounds to DNA. *Journal of molecular biology* **35**, 251-290 (1968).
37 Almaqwashi, A. A. *et al.* Strong DNA deformation required for extremely slow DNA threading intercalation by a binuclear ruthenium complex. *Nucleic Acids Res* **42**, 11634-11641 (2014).
38 Clark, A. G. *et al.* Reshaping the Energy Landscape Transforms the Mechanism and Binding Kinetics of DNA Threading Intercalation. *Biochemistry* **57**, 614-619 (2018).
39 Westerlund, F., Nordell, P., Nordén, B. & Lincoln, P. Kinetic characterization of an extremely slow DNA binding equilibrium. *The Journal of Physical Chemistry B* **111**, 9132-9137 (2007).
40 Nordell, P., Westerlund, F., Wilhelmsson, L. M., Nordén, B. & Lincoln, P. Kinetic Recognition of AT-Rich DNA by Ruthenium Complexes. *Angewandte Chemie International Edition* **46**, 2203-2206 (2007).
41 Ashkin, A. Acceleration and trapping of particles by radiation pressure. *Physical review letters* **24**, 156 (1970).
42 Chu, S., Bjorkholm, J., Ashkin, A. & Cable, A. Experimental observation of optically trapped atoms. *Physical review letters* **57**, 314 (1986).

43 Ashkin, A. & Dziedzic, J. M. Optical trapping and manipulation of viruses and bacteria. *Science* **235**, 1517-1520 (1987).
44 Ashkin, A., Dziedzic, J. M. & Yamane, T. Optical trapping and manipulation of single cells using infrared laser beams. *Nature* **330**, 769-771 (1987).
45 Ashkin, A. & Dziedzic, J. Internal cell manipulation using infrared laser traps. *Proceedings of the National Academy of Sciences* **86**, 7914-7918 (1989).
46 Ashkin, A., Schütze, K., Dziedzic, J., Euteneuer, U. & Schliwa, M. Force generation of organelle transport measured in vivo by an infrared laser trap. *Nature* **348**, 346-348 (1990).
47 Ashkin, A., Dziedzic, J. M., Bjorkholm, J. & Chu, S. Observation of a single-beam gradient force optical trap for dielectric particles. *Optics letters* **11**, 288-290 (1986).
48 Paramanathan, T. *Drug-DNA interactions at single molecule level: A view with optical tweezers*. (Northeastern University, 2010).
49 Williams, M. C. Optical tweezers: measuring piconewton forces. *Biophysics Textbook Online: http://www.biophysics.org/btol* (2002).
50 Wang, M. D., Yin, H., Landick, R., Gelles, J. & Block, S. M. Stretching DNA with optical tweezers. *Biophys J* **72**, 1335-1346 (1997).
51 Smith, S. B., Finzi, L. & Bustamante, C. Direct mechanical measurements of the elasticity of single DNA molecules by using magnetic beads. *Science* **258**, 1122-1126 (1992).
52 Lee, G. U., Chrisey, L. A. & Colton, R. J. Direct measurement of the forces between complementary strands of DNA. *Science* **266**, 771-773 (1994).
53 Williams, M. C. & Rouzina, I. Force spectroscopy of single DNA and RNA molecules. *Current opinion in structural biology* **12**, 330-336 (2002).
54 Zhang, Y., Ge, C., Zhu, C. & Salaita, K. DNA-based digital tension probes reveal integrin forces during early cell adhesion. *Nature Communications* **5**, 5167 (2014).
55 McCauley, M. J. & Williams, M. C. Mechanisms of DNA binding determined in optical tweezers experiments. *Biopolymers: Original Research on Biomolecules* **85**, 154-168 (2007).
56 Rouzina, I. & Bloomfield, V. A. Force-induced melting of the DNA double helix 1. Thermodynamic analysis. *Biophysical journal* **80**, 882-893 (2001).
57 Rouzina, I. & Bloomfield, V. A. Force-induced melting of the DNA double helix. 2. Effect of solution conditions. *Biophysical journal* **80**, 894-900 (2001).
58 van Mameren, J. *et al.* Unraveling the structure of DNA during overstretching by using multicolor, single-molecule fluorescence imaging. *Proceedings of the National Academy of Sciences* **106**, 18231-18236 (2009).
59 McCauley, M. J., Chaurasiya, K. R., Paramanathan, T., Rouzina, I. & Williams, M. C. DNA stretching as a probe for nucleic acid interactions: Reply to Comments on "Biophysical characterization of DNA binding from single molecule force measurements" by Kathy R. Chaurasiya, Thayaparan Paramanathan, Micah J. McCauley, Mark C. Williams. *Physics of life reviews* **7**, 358 (2010).
60 Bryden, N. *Quantifying the DNA Binding Properties of the Binuclear Ruthenium Complex ΛΛ-P*, Bridgewater State University, (2016).